

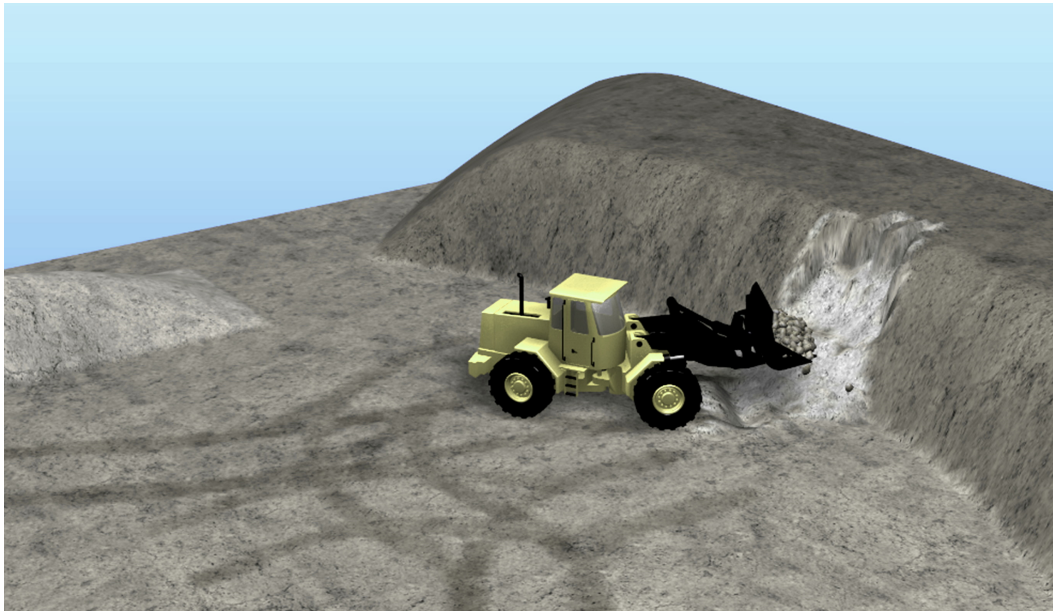
Tech report v. 1.01

agxTerrain

Tomas Berglund

Martin Servin

2019-03-05



Find the latest version of this report at
https://www.algoryx.se/download/agxTerrain_tech_report.pdf

Algoryx[®]

Algoryx Simulation AB, Umeå, Sweden

Abstract

This tech report describe the underlying theory and methodology for terrain dynamics in the multipurpose physics engine *AGX Dynamics*.

The model, **agxTerrain** , supports real-time simulation of soil and heavy equipment in strong coupling, and with rich dynamics and high precision. The soil can assume both solid, liquid and gas form depending on the level of agitation. This is realized through a multi-scale model that combines the standard continuum soil mechanics with particle and multi-body dynamics, representing only the essential degrees of freedom.

A number of different earth-moving operations can be simulated with realistic soil behavior and reaction forces on the tool and machine. These include bulldozing, compaction, digging, filling, grading, leveling and loading. The reaction forces on blades and buckets include both the soil separation force and penetration force, as well as inertial effects of the moving soil. The model support variable state of soil compaction and swelling, from the material being put under high contact stress or being fluidized. The soil strength and stiffness is also altered by this.

The key model parameters are the conventional bulk mechanical parameters of soil. A library of pre-calibrated soils is provided. The geometry of the tool, specifically its cutting edge (with or without teeth), separation plate and the back and side walls of a bucket are also important model parameters

Model validation and parameter calibration using high-resolution discrete element and multibody simulations is demonstrated. The examples show good agreement in soil dynamics and tool reaction forces between the realtime multiscale model and the high-resolution reference model.

Contents

1	Introduction	1
2	Theoretical background	1
2.1	Modelling framework	1
2.1.1	Rigid multibody dynamics	2
2.1.2	Contact dynamics	2
2.1.3	Nonsmooth discrete elements	3
2.1.4	Time-stepping scheme	4
2.1.5	Hybrid direct-iterative split solver	4
2.1.6	Time-step and solver iterations in NDEM simulations	5
2.2	Soil	5
2.2.1	Soil dynamics	6
2.3	Soil tool-interaction	7
2.3.1	Blade	8
2.3.2	Bucket	9
2.3.3	Penetration resistance	9
2.4	Stress distribution from a load	11
2.5	Variable soil compaction	11
2.5.1	Compressive strength	11
2.5.2	The effect of compaction on stiffness and shear strength	12
2.6	Previous work on terrain simulation models	12
3	agxTerrain	13
3.1	Outline of the agxTerrain model	13
3.1.1	Main algorithm	15
3.2	Assumptions and delimitations	16
3.3	Model components	17
3.3.1	Solid and fluidized terrain	17
3.3.2	Terrain surface heightfield	18
3.3.3	Subsoil stress from surface contacts	18
3.3.4	Soil compaction	18
3.3.5	Terrain equilibration	19
3.3.6	Digging tool	20
3.3.7	Soil deformer	21
3.3.8	Active zone	21
3.3.9	Conversion from solid mass	22
3.3.10	Particle creation, growth and mass exchange	22
3.3.11	Conversion from particles into solid mass	23
3.3.12	Soil particles	23
3.3.13	Aggregate bodies	24
4	Parametrization and calibration	24
4.1	Terrain parameter calibration	24
4.2	The direct shear test	25
4.3	Triaxial test	26
4.4	Terrain library	27
4.5	Digging tool parameter validation and calibration	28
5	Simulations	28
5.1	Excavation	28
5.2	Bulldozing	31

6 Conclusions

34

1 Introduction

High-performance simulation of heavy machines interacting with complex materials, such as rock and soil, is rewarding but challenging. Real-time performance is required for simulators with operators and hardware in the loop, which has important applications in operator training, human-machine interface development and experimental testing of new functions for automation.

The development of new machines and automation functions involve parameter studies and optimization in large design spaces. The breakthrough in recent years in deep learning is promising for a autonomous control with ability to generalize beyond the standard scenarios. However, the success of these techniques rely on access to large data-sets from many simulations. Running 100,000 simulations of 10 s duration require about 300 CPU hours of computing time, given that the simulations run at realtime. If the learning algorithm allow the simulations to be run mostly in parallel these numbers are manageable. But for harder problems, that require more and longer simulations, faster than realtime simulation is clearly needed. At the same time, it is important that the simulation models have faithful physics and rest on a solid mathematical foundation such that the level of realism can be verified and controlled. Furthermore, the involved models and algorithms should be easy for the user to understand, parameterize and validate through domain knowledge and empirical test data. These are important features for a solution to be transferable from simulation to the real system.

This report present a new solution for computational modelling and realtime simulation of terrain dynamics under the interaction with heavy equipment vehicles. The development is driven by, but not limited to, the need for simulation-based development of autonomous capabilities in earthmoving equipment as well as operator training.

Algoryx is a global technology leader in high-fidelity realtime physics and multibody simulation of complex machines. *AGX Dynamics* is a multi-purpose physics engine for simulators, VR applications, engineering and scientific simulation of mechatronics, materials and industrial processes. Typical systems include vehicles, robots, cranes and other complex mechanisms found in manufacturing, transportation, construction and bulk material processing. Realtime deformable terrain has been available since 2012. Development of a next generation of realtime terrain, with unprecedented grade of fidelity and realism, was initiated in 2018. The new solution, described in this report, is referred to as **agxTerrain**.

2 Theoretical background

The **agxTerrain** is a multi-scale model based multibody systems dynamics, the discrete element method (DEM) and continuum soil mechanics. Textbooks that provide a relevant background include *Dynamics of Multibody Systems* by Shabana [52], *Granular Media: Between Fluid and Solid* by Andreotti, Forterre and Polouquen [3], *An Introduction to Soil Mechanics* [58] by Verruijt, *Soil Cutting and Tillage* by MckYes [34] and *Theory of Ground Vehicles* by Wong [64].

2.1 Modelling framework

It is a common approach to model vehicles and mechanical devices as rigid multibody systems and to use the discrete element method (DEM) for modelling of soil. The physics engine *AGX Dynamics* rest on a modelling and simulation framework based on discrete variational mechanics with nonsmooth dynamics. It support multidomain and multiphysics simulation with particular emphasis on multibody dynamics. The AGX framework for modelling and simulation enables fast and stable simulations using time integration with fixed and large time-step [30], typically 17 ms (60 Hz).

2.1.1 Rigid multibody dynamics

The state of a rigid multibody system with N_b bodies, N_j joints and actuators and N_c contacts, is represented on descriptor form in terms of the system position, $\mathbf{x}(t) \in \mathbb{R}^{6N_b}$, velocity, $\mathbf{v}(t) \in \mathbb{R}^{6N_b}$, and Lagrange multipliers, $\boldsymbol{\lambda}_j(t) \in \mathbb{R}^{6N_j}$ and $\boldsymbol{\lambda}_c(t) \in \mathbb{R}^{6N_c}$, that are responsible for the constraint forces in joints and contacts. The system position variable is a concatenation of the spatial and rotational coordinates of the N_b bodies, $\mathbf{x} = [\mathbf{x}, \mathbf{e}]$, and the velocity vector holds the linear and angular velocities, $\mathbf{v} = [\mathbf{v}, \boldsymbol{\omega}]$. The time evolution of the multibody system state variables $[\mathbf{x}, \mathbf{v}, \boldsymbol{\lambda}]$ is given by the following set of equations

$$\mathbf{M}\dot{\mathbf{v}} = \mathbf{f}_{\text{ext}} + \mathbf{G}_j^T \boldsymbol{\lambda}_j + \mathbf{G}_c^T \boldsymbol{\lambda}_c \quad (1)$$

$$\varepsilon_j \boldsymbol{\lambda}_j + \eta_j \mathbf{g}_j + \tau_j \mathbf{G}_j \mathbf{v} = \mathbf{u}_j, \quad (2)$$

$$\text{contact_law}(\mathbf{v}, \boldsymbol{\lambda}_c, \mathbf{g}_c, \mathbf{G}_c), \quad (3)$$

where \mathbf{f}_{ext} is the external force, which like the constraint forces, $\mathbf{G}_j^T \boldsymbol{\lambda}_j$ and $\mathbf{G}_c^T \boldsymbol{\lambda}_c$, have dimension \mathbb{R}^{6N_b} and is composed of linear force and torque. The system mass matrix is $\mathbf{M} \in \mathbb{R}^{6N_b \times 6N_b}$. Eq. (2) is a generic constraint equation. An ideal joint is can be represented with $\varepsilon_j = \tau_j = \mathbf{u}_j = 0$, in which case Eq. (2) express a holonomic constraint, $\mathbf{g}_j(\mathbf{x}) = 0$. A linear or angular motor may be represented by a velocity constraint $\mathbf{G}_j \mathbf{v} = \mathbf{u}_j(t)$ with set speed $\mathbf{u}_j(t)$, which follows by setting $\varepsilon_j = \eta_j = 0$ and $\tau_j = 1$. In the general case, Eq. (2) model a joint with constraint function $\mathbf{g}_j(\mathbf{x})$, Jacobian $\mathbf{G} = \partial \mathbf{g} / \partial \mathbf{x}$, joint compliance ε_j and viscous damping rate τ_j . The holonomic and nonholonomic constraints can be seen as the limit of a stiff potential, $\mathcal{U}_\varepsilon = \frac{1}{2\varepsilon} \mathbf{g}^T \mathbf{g}$, or a Rayleigh dissipation function, $\mathcal{R}_\tau = \frac{1}{2\tau} (\mathbf{G}\mathbf{v})^T \mathbf{G}\mathbf{v}$, respectively. This offer the possibility of mapping known models of viscoelasticity to the compliant constraints. Descriptor form means that no coordinate reduction is made. The system is represented explicitly with its full degrees of freedom, although the presence of constraints. This is necessary for non-ideal joints and for dynamic contacts at arbitrary locations.

2.1.2 Contact dynamics

We consider the system to have *nonsmooth dynamics* [1]. That means that the velocity and Lagrange multipliers are allowed to be discontinuous in time, reflecting instantaneous changes from impacts, frictional stick-slip transitions or joints and actuators reaching their limits. This is unavoidable when using an implicit integration scheme¹ because of the coupling between the state variables trough the contact law Eq. (3).

As contact law between particles we use a model that include cohesive-viscoelastic normal contacts (n), tangential Coulomb friction (t) and rolling resistance (r). These are formulated in terms of inequality and complementarity conditions for the velocities, Lagrange multipliers an constraint functions. The resulting model can be seen as a time-implicit version of conventional discrete element method (DEM) and is therefore referred to as nonsmooth DEM (NDEM) [45, 50]. We use the following conditions as `contact_law`:

$$0 \leq \varepsilon_n \boldsymbol{\lambda}_n + \mathbf{g}_n + \tau_n \mathbf{G}_n \mathbf{v} \perp (\boldsymbol{\lambda}_n + \bar{\boldsymbol{\lambda}}_c) \geq 0, \quad \bar{\boldsymbol{\lambda}}_c \equiv c_p A_p / |\mathbf{G}_n^T| \quad (4)$$

$$\gamma_t \boldsymbol{\lambda}_t + \mathbf{G}_t \mathbf{v} = 0, \quad |\boldsymbol{\lambda}_t| \leq \mu_t |\mathbf{G}_n^T \boldsymbol{\lambda}_n| \quad (5)$$

$$\gamma_r \boldsymbol{\lambda}_r + \mathbf{G}_r \mathbf{v} = 0, \quad |\boldsymbol{\lambda}_r| \leq r \mu_r |\mathbf{G}_n^T \boldsymbol{\lambda}_n|, \quad (6)$$

where \mathbf{g}_n is a function of the contact overlap and the Jacobians, \mathbf{G}_n , \mathbf{G}_t and \mathbf{G}_r govern the normal, tangent and rotational directions of the contact forces [50]. The parameters ε_n , τ_n , γ_t in Eq. (4) control the contact compliance and damping, and $\bar{\boldsymbol{\lambda}}_c$ the cohesion. Setting these parameters to zero means that no penetration should occur, $\mathbf{g}_n(\mathbf{x}) \geq 0$, and if so the

¹The alternative is to resolve the contact events using smooth trajectories, stiff potentials and small time-step explicit time integration. In the limit of high stiffness and small mass, the simulation time increase indefinitely with this approach.

normal force should be repulsive, $\lambda_n \geq 0$. The inclusion of $\bar{\lambda}_c$ enables cohesive normal force with maximum value $f_c^{\max} = c_p A_p$, where c_p is the particle cohesion and A_p is the particle cross section area. The cohesion is active when the contact overlap is smaller than a certain *cohesive overlap*, with recommended value $\delta_c = 0.025d$. This reduces the effective size of the particles correspondingly. Eq. (5) state that contacts should have zero slide velocity, $\mathbf{G}_t \mathbf{v} = 0$, giving rise to a friction force that is bounded by the Coulomb friction law with friction coefficient μ_t . Similarly, Eq. (6) states that, as long as the constraint torque is no greater than the rolling resistance law, relative rotational motion of contacting bodies is constrained, $\mathbf{G}_r \mathbf{v} = 0$. Here, μ_r is the rolling resistance coefficient and r is the particle radius.

We separate collisions into resting contacts and impacts using an impact threshold velocity v_{imp} . If the relative contact velocity is smaller than this value the contacts are modelled as described above. In case of impacts we apply the Newton impact law

$$\mathbf{G}_n \mathbf{v}^+ = -e \mathbf{G}_n \mathbf{v}^-, \quad (7)$$

with restitution coefficient e , while preserving all other constraints in the system on the velocity level, $\mathbf{G} \mathbf{v}^+ = 0$. This is carried out in an impact stage solve, prior to the main solve for the constrained equations of motions (1)-(3). With this division, the restitution coefficient become the key parameter for modelling the dissipative part of the normal force. For the resting contacts we can simply enforce numerical stability using $\tau_n = 4.5\Delta t$ with little consequence of the damping being artificially strong [61].

2.1.3 Nonsmooth discrete elements

We map the normal contact law, Eq. (4), to the non-linear Hertz-Mindlin contact model, which follows from the theory of linear elasticity [23]. In that model the normal force is split into an nonlinear spring and viscous damper force

$$\mathbf{f}_n = k_n \delta^{3/2} \mathbf{n} + k_n c_d \delta^{1/2} \dot{\delta} \mathbf{n}, \quad (8)$$

where $\delta(\mathbf{x})$ and $\dot{\delta}(\mathbf{x})$ is the contact overlap and penetration velocity of a pair of contacting spherical particles. The spring stiffness and damping coefficients are

$$k_n = \frac{E\sqrt{2d^*}}{3(1-\nu^2)}, \quad c_d = \frac{4(1-\nu^2)(1-2\nu)\eta}{15E\nu^2}, \quad (9)$$

where E is the Young's modulus, ν is Poisson's ratio and η is the material viscosity constant. The effective diameter between two interacting spheres, a and b , with diameter d_a and d_b is $d^* = (d_a^{-1} + d_b^{-1})^{-1}$. The mapping to Eq. (4) is accomplished by $g_n = \delta^{5/4}$, $\varepsilon_n = 5/4k_n$ and $\tau_n = \max(5c_d/4, 4.5\Delta t)$. In the limit of small time-step, $5c_d/4 > 4.5\Delta t$, the Newton impact law can be dropped and the damping be resolved using the dissipative part of the Hertz model.

The particle shape is an important material parameter for granular matter and soil. Particle angularity can have significant effect on the bulk internal friction and on the angle of repose. Complex particle shape is, however, also associated with increased computational complexity in simulations. Both the number of contacts and the time for computing each contact point increase with more complex shapes. It has been shown, both theoretically and experimentally, that many effects of particle angularity can be modelled with spherical particles possessing rolling resistance [42, 12, 15, 62]. As pointed out in [12], a n -sided polygon exhibit a rolling dilatancy angle $\psi = \pi/2n$ that lead to rolling resistance torque, $\tau_r \leq \mu_r(d/2)|\mathbf{f}_n|$, with rolling resistance coefficient $\mu_r = (1/4) \tan \psi$. This formula predicts $\mu_r = 0.05$ for an eight-sided polygon ($n = 8$), $\mu_r = 0.1$ for a square ($n = 4$) and $\mu_r = 0$ for a sphere ($n = \infty$). This is illustrated in Fig. 1.

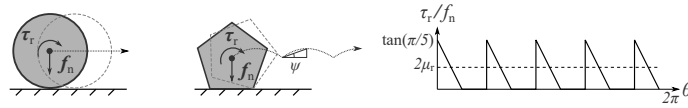


Figure 1: Illustration of the relationship between polygon shape and rolling resistance, reproduced from [12].

2.1.4 Time-stepping scheme

Equation (1) and (2) form a set of differential algebraic equations (DAE) for the system variables $[\mathbf{x}, \mathbf{v}, \boldsymbol{\lambda}]$. Unfortunately, DAEs are prone to numerical instability. The theory of discrete variational mechanics offers a way to construct time-stepping algorithms with symmetry-preserving properties for mechanical systems. The key is to introduce discrete time already for the Lagrangian and action principle. The important symmetry properties, e.g., preservation of energy and momentum, can this way be built into the numerical scheme by design. The symplectic property of these integrators guarantee numerical stability and produce numerical solutions that shadow the exact trajectory with global bounds that depend on the time-step size. In many simulations of dynamical systems these properties are more important than high local resolution with an integrator that may diverge globally with time. SPOOK [28] is a first order accurate discrete variational integrator, developed particularly for fixed time-step realtime simulation with non-ideal constraints, like Eq. (1)-(2). It has been proven to be linearly stable. The numerical time integration scheme for computing the position, velocity and Lagrange multiplier, $[\mathbf{x}_{i+1}, \mathbf{v}_{i+1}, \boldsymbol{\lambda}_{i+1}]$ at time $t_{i+1} = t_i + \Delta t$ from previous state, $[\mathbf{x}_i, \mathbf{v}_i]$, at time t_i consist of a position update

$$\mathbf{x}_{i+1} = \mathbf{x}_i + \Delta t \mathbf{v}_{i+1}, \quad (10)$$

after having computed the new velocity and Lagrange multiplier $\mathbf{z} = [\mathbf{v}_{i+1}, \boldsymbol{\lambda}_{i+1}]$ by solving the following mixed complementarity problem (MCP) [36]

$$\begin{aligned} \mathbf{H}\mathbf{z} + \mathbf{b} &= \mathbf{w}_l - \mathbf{w}_u \\ 0 &\leq \mathbf{z} - \mathbf{l} \perp \mathbf{w}_l \geq 0 \\ 0 &\leq \mathbf{u} - \mathbf{z} \perp \mathbf{w}_u \geq 0 \end{aligned} \quad (11)$$

where

$$\mathbf{H} = \begin{bmatrix} \mathbf{M} & -\mathbf{G}_j^T & -\mathbf{G}_n^T & -\mathbf{G}_t^T & -\mathbf{G}_r^T \\ \mathbf{G}_j & \boldsymbol{\Sigma}_j & 0 & 0 & 0 \\ \mathbf{G}_n & 0 & \boldsymbol{\Sigma}_n & 0 & 0 \\ \mathbf{G}_t & 0 & 0 & \boldsymbol{\Sigma}_t & 0 \\ \mathbf{G}_r & 0 & 0 & 0 & \boldsymbol{\Sigma}_r \end{bmatrix}, \mathbf{z} = \begin{bmatrix} \mathbf{v}_{i+1} \\ \boldsymbol{\lambda}_j \\ \boldsymbol{\lambda}_n \\ \boldsymbol{\lambda}_t \\ \boldsymbol{\lambda}_r \end{bmatrix}, \mathbf{b} = \begin{bmatrix} -\mathbf{M}\mathbf{v}_i - \Delta t \mathbf{M}^{-1} \mathbf{f}_{\text{ext}} \\ -\boldsymbol{\omega}_j + \frac{4}{\Delta t} \boldsymbol{\Upsilon}_j \mathbf{g}_j - \boldsymbol{\Upsilon}_j \mathbf{G}_j \mathbf{v}_i \\ \frac{4}{\Delta t} \boldsymbol{\Upsilon}_n \mathbf{g}_n - \boldsymbol{\Upsilon}_n \mathbf{G}_n \mathbf{v}_i \\ 0 \\ 0 \end{bmatrix}. \quad (12)$$

For notational convenience, a factor Δt has been absorbed in the multipliers such that the constraint force reads $\mathbf{G}^T \boldsymbol{\lambda} / \Delta t$. The upper and lower limits, u and l , in Eq. (11), follow from the contact law and joint and motor limits. Since the limits depend on the solution, this is a partially nonlinear complementarity problem. The slack variables w_l and w_u are used only internally by the MCP solver only. The regularization and damping terms are given by $\boldsymbol{\Sigma}_n = 4\varepsilon_n / \Delta t^2 (1 + 4\frac{\tau_n}{\Delta t})$, $\boldsymbol{\Sigma}_t = \gamma_t / \Delta t$, $\boldsymbol{\Sigma}_r = \gamma_r / \Delta t$ and $\boldsymbol{\Upsilon}_n = 1 / (1 + 4\frac{\tau_n}{\Delta t})$.

2.1.5 Hybrid direct-iterative split solver

AGX has both direct and iterative MCP solvers that are tailored for the sparse linear algebra operations of contacting multibody systems. The direct solver is needed for vehicle dynamics and power transmission, characterized by large mass ratios and high stiffness that lead to equations with large condition number. The direct solver is a sparse direct block-pivot LDLT solver [29] and is exact to machine precision. The scalable iterative solver provides a fast and approximate solution of granular dynamics. The coupling can be

solved either using a direct or iterative method, or a combination. AGX is equipped with a hybrid direct-iterative solver with a smart splitting scheme. This support the simultaneous use of both type of solvers for simulating coupled system, with different precision in the sub-system solutions. The result is simulations that combine high performance, accuracy and scalability

The dynamics of the granular material is solved to lower precision using a projected Gauss-Seidel (PGS) solver for the MCP [50]. To accelerate the PGS solver computations, we employ domain decomposition for parallel processing, warmstarting [59] and model reduction [49].

2.1.6 Time-step and solver iterations in NDEM simulations

For a given error tolerance ϵ in a NDEM simulation, the time-step should be chosen [51]

$$\Delta t \lesssim \min(\epsilon d/v_n, \sqrt{2\epsilon d/\dot{v}_n}) \quad (13)$$

where v_n is the normal contact velocity and \dot{v}_n is the largest potential acceleration that can occur from the forces acting on a particle. In a dense packing with mean stress σ the potential acceleration can be estimated by $\dot{v}_n \sim \sigma A_p/m_p$, with particle cross-section $A_p = \pi d^2/4$, mass m_p . In the absence of external loads, from which the stress can be estimated from, the potential acceleration can be estimated with the gravity acceleration.

The required number of projected Gauss-Seidel iterations has been found empirically to satisfy the relation [51]

$$N_{it} \gtrsim 0.1n/\epsilon \quad (14)$$

where n is the length of the contact network (number of particles) in the direction of the dominant stress. When warm-starting is applied, this can be reduced by a factor 2 to 5 [60].

Example 1. Choose an error tolerance of $\epsilon = 0.05$, and consider a system with $v_n \approx 1$ m/s, particle diameter $d_p = 0.05$ m, mass $m_p = 0.2$ kg confined in a cubic container with side length $L = 1.0$ m and wall pressure σ . For a pressure of $\sigma = 1.0$ kPa the acceleration become $\dot{v}_n = 10$ m/s² and the time-step limits $\Delta t \lesssim \min(50, 20)$ ms. For the larger pressure $\sigma = 100$ kPa we $\Delta t \lesssim 2$ ms. Since the side-length is $n \sim 20$ particle diameters, the number of iterations become $N_{it} \gtrsim 40$.

2.2 Soil

Soil is the relatively loose layer of material resting on the bedrock [11, 58]. It is a heterogeneous media consisting of a mixture of mineral particles of different size and shape, containing some amount of moisture and gas. Sometimes the presence of organic matter is substantial and important for the mechanical properties, e.g., fiber-reinforcement by roots. In the presence of fine particles ($< 100\mu\text{m}$) and moisture, the attractive interparticle forces (due to surface tension) become comparable in size to the repulsive forces and the material behave cohesive, i.e., exhibit resistance to tensile deformations and additional shear strength to that from the particle friction and interlocking. Clay and silt are cohesive soils that are distinguished by particle size. In the absence of fine particles or moisture the soil become cohesionless, also known as *friction soil*, and is considered to be a granular material [3]. Sand, gravel and cobbles are examples of cohesionless soil. A general soil has a particle size distribution that may include all of the mentioned types.

Cohesionless soil exhibit shear resistance due to particle friction and interlocking from strong normal force network. The particle friction force is limited by the Coulomb law. Therefore, if the normal stress increase, the shear resistance of the bulk increase correspondingly. The critical ratio over shear stress and normal stress where a material fail is known as the *internal friction*. It depends on the interparticle surface friction, on the

particle shape and packing ratio. Shearing can normally not occur without the material expanding at the same time, known as *dilatancy*. Therefore, confined and densely packed materials can be very strong. The angle of repose, i.e. the maximum stable slope of a pile, coincide well with the internal friction angle (of loosely packed materials).

The water content has major impact on the mechanical properties for fine-grained soils. At low moisture level, the material may appear as a brittle solid (due to attractive chemical bonds, cementation, in addition to friction). When the water content exceeds the so called *plastic limit* it behaves like a plastic solid. If the moisture level exceeds the *liquid limit* it transitions to a non-Newtonian fluid. The reason is that in a saturated soil, the liquid and particles share the normal stress, i.e., the hydrostatic pressure mediated by the nearly incompressible liquid relieve the normal stress on the particles from the contact network. As a consequence, the maximum interparticle friction force decrease. The *effective stress* is simply the total stress subtracted by the pore pressure. Thus, a stable soil structure can lose its bearing capacity just by an increase in pore pressure, e.g., due to rainfall. Conversely, a negative pore pressure increases the strength of the material. This is what give the initial strength to a sandcastle. As it dries, the pore pressure suction is lost, and it collapses more easily.

2.2.1 Soil dynamics

Like granular media, soil can exist in either solid, fluid or gaseous state. Due to strong dissipation, the soil transitions quickly from gas to fluid to solid unless there is a sufficient level of external agitation (vibrations or a moving tool) or during the escape from a metastable state (slope failure). There is no general theory for soil dynamics that describe both the solid, fluid and gaseous state. In the solid regime, the material may be modelled as an elastoplastic solid. In the fluid regime, where the rate of strain and deformations are large, the dynamics is better modelled using a non-Newtonian fluid model. The gaseous regime requires either multiphase fluid description, kinetic theory or resolution of the individual particles, e.g., by discrete elements. The latter two are, however, too computational intense for real-time simulation of large domains.

On large length-scales, relative to particle size, a soil may be modelled using continuum mechanics. When the stresses are below a certain *yield strength* condition, it behaves as an *elastic solid* according to some constitutive relating stress to strain, e.g., Hooke's law. When the stresses reach the yield condition the solid fails. If the material deforms quasistatically it may be modelled as an *elastoplastic solid*, with a certain *plastic flow rule*. The solid may fracture by *brittle failure* (for clay and silt with water content below the *plastic limit*).

The governing equations in continuum mechanics are the *momentum balance equation*

$$\rho[\partial_t + \mathbf{u} \cdot \nabla] \mathbf{u} = \nabla \cdot \boldsymbol{\sigma} + \rho \mathbf{f}_{\text{ext}}, \quad (15)$$

and the *mass continuity equation*

$$\partial_t \rho + \nabla \cdot [\rho \mathbf{u}] = 0, \quad (16)$$

where $\mathbf{u}(\mathbf{x})$ is the velocity field and $\rho(\mathbf{x})$ is the mass density field. The equation system is closed with some *constitutive equation* for the stress $\boldsymbol{\sigma}(\mathbf{x})$. In the regime of linear elastic deformations the Hooke's law applies, $\boldsymbol{\sigma} = \mathbf{C}\boldsymbol{\epsilon}$, where $\boldsymbol{\epsilon}(\mathbf{x})$ is the strain tensor. For a linear viscous fluid, the stress is depends linearly on the rate of strain $\dot{\boldsymbol{\epsilon}} = \frac{1}{2}[\nabla^T \mathbf{u} + \nabla \mathbf{u}^T]$.

The simplest yield condition for soil is the *Mohr-Coulomb* criteria. It predicts that a rigid or elastic continuum will fail along any plane with normal \mathbf{n} where the stress satisfies

$$\tau_{\mathbf{n}} = \tan(\phi)\sigma_{\mathbf{n}} + c, \quad (17)$$

where the normal stress is $\sigma_{\mathbf{n}} = \boldsymbol{\sigma}_{\alpha\beta} n_{\beta}$ and the shear stress is $\tau_{\mathbf{n}} = \sqrt{(\boldsymbol{\sigma} \cdot \mathbf{n})^2 - \sigma_{\mathbf{n}}^2}$. The model has two parameters for the strength of the material. the *angle of internal friction*,

ϕ , and the cohesion, c . Analogously with Coulomb friction, the critical shear strength grows linearly with the normal stress (pressure). At zero pressure the shear stress must also overcome the cohesive strength of the material.

The *Drucker-Prager* yield criteria is a 3D generalization of Mohr-Coulomb, with the advantage of being a smooth failure surface. It is conventionally expressed in terms of the stress invariants as

$$\sqrt{J_2} = \frac{\eta}{3}I_1 + \xi c, \quad (18)$$

where $I_1 = \text{tr}(\boldsymbol{\sigma})$ is the first invariant of the stress tensor, $J_2 = 0.5\text{tr}(\bar{\boldsymbol{\sigma}}^2)$ is the second invariant of the deviatoric stress tensor $\bar{\boldsymbol{\sigma}} = \boldsymbol{\sigma} - \frac{1}{3}I_1\mathbf{1}$, and $\eta = 6 \sin \phi / \sqrt{3} (3 - \sin \phi)$ and $\xi = 6 \cos \phi / \sqrt{3} (3 - \sin \phi)$. There are extensions of the Drucker-Prager model with a cap at large pressure for modelling dynamic compaction.

Soil materials can form piles and slopes with surface inclination up to a critical angle of repose. For cohesion-free materials the angle of repose coincides well with the internal friction angle. With cohesion it may be larger [35]. Small piles may be as steep as 90 degrees. In large piles the gravity force dominate over the cohesion, $c/\rho gh \cos(\phi) \ll 1$ with pile height h , and the angle of repose depend primarily on the internal friction. With a high moisture content, the effective normal stress decrease and the angle of repose with it. If the angle of repose is exceeded, or if a load is applied which cause the deviatoric stress to increases more than the normal stress, the material fails and start flowing. The same happens if the moisture content increases.

Quasistatic deformations at the plastic yield surface, $\Phi(\boldsymbol{\sigma}) = 0$, can be described by an elastoplastic model for the stress increment, $d\boldsymbol{\sigma} = \mathbf{C}(d\boldsymbol{\epsilon} - d\boldsymbol{\epsilon}^P)$, with a plastic flow rule for the plastic strain increment (possibly with kinematic constraint), $d\boldsymbol{\epsilon}^P = \lambda \partial_{\boldsymbol{\sigma}} \Psi$, with plastic potential function $\Psi(\boldsymbol{\sigma})$ and plastic multiplier λ (to be solved for). Other elastoplastic constitutive law is the Cam-clay model. Numerical integration schemes for the plastic flow can be found in [38].

In the liquid regime, the material may be described as a non-Newtonian fluid with particular constitutive law between stress and strain-rate, e.g. as a Bingham-fluid. The so-called $\mu(I)$ rheology models describes dense granular flow as an non-Newtonian fluid with internal friction, modelled as viscosity, being a function of the inertial number [44, 24]. This model shows very good agreement with experiments and require few parameters for spherical particle systems. However, there is currently no way of extending the model to particles with a distribution in size and shape.

Landslides, debris flow and avalanches has attracted particular attention and there are dedicated models for describing their dynamics [2, 18, 19]. A gravity driven rapid shear flow drives particle segregation. Large particles and boulders are transported to the top and front of the flow [14].

2.3 Soil tool-interaction

By soil-tool interaction we mean the displacement or material flow that is induced by a tool of particular shape and motion, and the reaction force exerted by the soil on the tool. Example of different tools include blade, bucket, cone, drum roller, plow, ripper and wedge. Critical stresses cause shear failure. In soil-tool interaction the failure is often localized along a well-defined failure surface, a phenomena known as *strain localization* or *shear band formation*. The failure surface can be estimated from the theory of elastoplasticity and critical states for certain states of stationary equilibrium between a tool and a soil. Examples are found in [34] and [13]. We refer to the region confined by the tool, failure surface and the free surface as the *active zone*.

2.3.1 Blade

A blade, or *separating plate*, has two basic modes of operation, *penetration* and *separation*. Penetration is the motion straight into the soil with relative velocity in tangential direction of the plate only. It does not lead to significant deformation, as soil is displaced only locally to make space for the penetrating plate. The penetration resistance caused by the soil-tool friction and confining pressure may nevertheless be significant. Separation corresponds to movement normal to the plate and is the main cause of soil failure and large displacements. The edge where the blade meet the material is referred to as the *cutting edge*. See Fig. 2

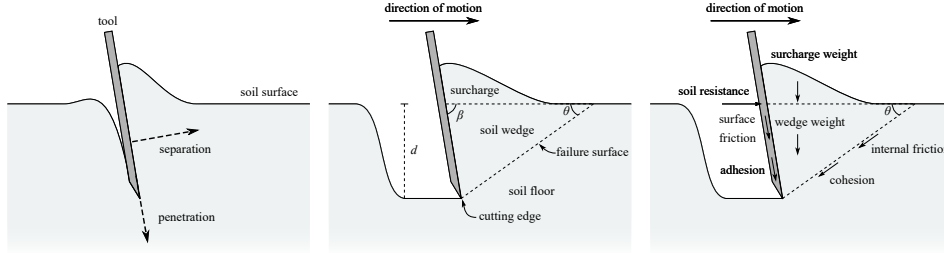


Figure 2: Illustration of a blade interacting with a soil. There are two modes of operation, penetration and separation (left). The formation of a wedge shaped active zone (middle). The soil resistance when a blade pushes the soil (right).

The cutting and pushing of soil with a wide blade has been thoroughly investigated analytically, experimentally and numerically [34, 25, 40, 48, 53, 57]. It is a combination of penetration and plate separation. The latter is the dominant force in most bulldozing situations and the penetration resistance is often neglected in such applications.

The shape of the failure surface can be computed analytically in the two dimensional case, applicable for a wide blade, using the method of stress characteristics and assuming the Mohr-Coulomb criteria [34]. The failure surface is often approximated with a plane. This defines an *active zone* with the shape of a wedge. Rankine's theory [3] for a flat soil with a blade pushing on it in the horizontal direction predicts that the soil fails at an angle $\theta = \pi/4 - \phi/2$ against the horizontal. In three dimensions, the failure surface extends sideways also, which cause long berms along the sides of a pushing blade.

The separation force acting on the blade when moving at a constant speed is well described using the *Fundamental Earthmoving Equation* (FEE) [46]. The FEE is motivated by wedge model of the soil failure. The force resistance per tool width L , in the FEE is composed of four terms

$$\frac{F}{L} = \rho g d^2 N_\gamma + Q N_Q + c d N_c + c_a d N_a, \quad (19)$$

with specific soil mass density ρ , tool penetration depth d , soil cohesion c , surcharge force Q (per tool width) and soil-tool adhesion c_a . The first term is the due to the weight of the wedge, the second term is the additional (vertical) surcharge, the third term the cohesive force in the failure surface, and the fourth term is the resistance due the adhesion between the blade and the soil. The four N -factors (found in the listed literature) depend of the geometry failure zone, the tool geometry, the internal friction and the soil-tool surface friction. The quadratic dependency on the cutting depth d reflect that the weight depends linearly on the cross-section area of the failure zone. Note that the cohesive and adhesive force terms are proportional to the area of the failure surface and blade contact surface, respectively. One key limitation of the FEE is that it assumes stationary equilibrium and low speed of the blade and soil flow.

2.3.2 Bucket

An excavator or wheel loader bucket is basically composed of a *ground plate*, a curved *back plate* and two *side plates*, see Fig. 3. The ground plate functions as a separating plate with a cutting edge. Just like the bulldozer blade, it is responsible for cutting through the soil and separating it. The cutting edge is often equipped with pointed *teeth* that facilitates the penetration into the soil surface. According to McKyes [34], the side-walls constrain the soil failure to the forward direction, i.e., to behave more like for a wide blade than a narrow blade.

As the bucket is filled, a *dead load* of immobile soil is formed in the back of the bucket. This form an implicit, *secondary separation plate*. It is pointed out by Park [41] that it is important to capture the transition from a primary to a secondary separating plate when modelling the soil displacement and reaction force for buckets.

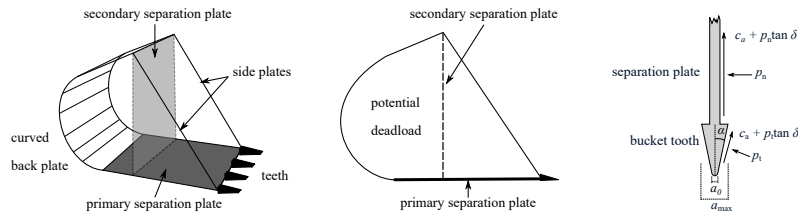


Figure 3: The basic design of a bucket with the primary and secondary separation plates indicated is illustrated in the left and middle images (reproduced from [41]). The penetration force on the teeth and primary separation plate are shown in the right image.

A review of resistive force models for excavation machines is provided in [7]. Blouin divide the fundamental earthmoving action into *penetration*, *cutting* (or separation) and *loading* (or excavation). The cutting phase is considered to be a lateral motion with constant rake angle, which is the inclination of the bucket. This is basically a bulldozing operation. The force resistance is therefore modelled using the FEE alone or in combination with a penetration force.

The FEE is, however, only applicable under limited conditions. It does not apply directly to soil separation in sloped terrain. Also, the FEE does not automatically consider the formation of a secondary separation plate by the accumulated dead load of material in the bucket. This act like a pushing blade with an inclination that may be very different from that of the ground plate. Extensions of the FEE to sloped terrain is provided in [32, 6] and in more detail later in the thesis of Park [41], based on the passive earth pressure theory. Park suggest the following failure angle between the failure plane and possibly inclined soil surface is

$$\theta_{\text{Park}} = \left(\frac{\pi}{4} - \frac{\phi + \delta}{2} \right) + \left(\frac{\pi}{4} - \frac{\beta}{2} \right), \quad (20)$$

where $\delta = \arctan(\mu_{\text{tool}})$ is the soil-tool surface friction angle and β is the angle of the separation plate relative to the soil surface.

2.3.3 Penetration resistance

Pure penetration occurs when a thin tool moves straight into the terrain, displacing only the soil necessary for fitting the tool. Buckets are sometimes penetrated deep into the soil before separation (cutting) starts. In strong soil, the penetration resistance may also be significant throughout the cutting phase.

The penetration resistance experienced by a tool consists of two main parts: from the teeth (or edge) and from the primary separating plate [6, 41]. The situation is illustrated in Fig. 3. The resistance from the separating plate contacting the soil is simply modelled

by a frictional force proportional to the passive earth pressure in the soil. There may also be adhesion force acting in tangential direction. Park model these two forces by [41]

$$f_{ps} = (c_a + \mu_{\text{tool}}p_n)A_s \quad (21)$$

where c_a is the adhesion between soil and plate, p_n is the normal pressure on the soil plate, μ_{tool} is the friction between the soil and the plate, and A_s the area of the separating plate penetrating the soil. The normal pressure is given by Bennett et al. [6] as

$$p_n = \frac{1}{2}\rho gz [(1 + K_0) + (1 - K_0) \cos(2\beta)], \quad (22)$$

where K_0 is the coefficient of lateral earth pressure, ρ is the specific soil mass density, z is the penetration depth and β is the insertion angle. A simple model for the coefficient of lateral earth pressure is given by Jaky [21] as $K_0 = 1 - \sin \phi$.

The resistance due to the tool's teeth can be modelled in a similar way

$$f_{pt} = n_t [p_t + (c_a + \mu_{\text{tool}}p_t) / \tan \alpha] A_t \quad (23)$$

where n_t is the number of teeth with cross-section area A_t and tooth angle α . The major difference is that the pressure at the teeth, p_t , is not the same as the passive earth pressure. The teeth experience a higher pressure because they are actively deforming the soil to accommodate the full size of the teeth. When the teeth have fully penetrated the soil it is assumed that enough space has been created for the complete separating plate to fit.

The pressure on the teeth during penetration can be modelled using the *finite cavity expansion model* by Yu and Houlsby [66], which assumes a linear elastoplastic soil model with a Mohr-Coulomb yield criterion. The model explains how a soil cavity of size a grows and the pressure p_t required for making it grow further by radial expansion. The material parameters are Young's modulus E , Poisson ratio ν , internal friction angle ϕ , cohesion c and angle of dilation ψ . The tool teeth is assumed to have diameter a_0 at the tip and a_{max} at the base. The tooth pressure, p_t , is solved from the *cavity pressure ratio*

$$R = \frac{(m + \bar{\alpha})[\bar{Y} + (\bar{\alpha} - 1)p_t]}{\bar{\alpha}(1 + m)[\bar{Y} + (\bar{\alpha} - 1)p_0]} \quad (24)$$

where $p_0 = \rho gz$ is the lateral earth pressure, m distinguish between cylindrical ($m = 1$) and spherical ($m = 2$) cavity expansion, and the parameters $\bar{\alpha}$ and \bar{Y} are defined in Appendix A. Before Eq. (24) can be solved for p_t , one must solve cavity pressure ratio, R , from the following pressure expansion relationship

$$\frac{a}{a_0} = \left[\frac{R^{-\bar{\gamma}}}{(1 - \bar{\delta})^{\frac{\bar{\beta}}{\beta+m}} - \frac{\bar{\gamma}}{\bar{\eta}} \Lambda_1(R, \bar{\xi})} \right]^{\frac{\bar{\beta}}{\beta+m}} \quad (25)$$

where $a \in [a_0, a_{\text{max}}]$ is the current cavity size depending on the penetration depth and the parameters $\bar{\beta}$, $\bar{\gamma}$, $\bar{\delta}$, $\bar{\eta}$, $\bar{\xi}$ and G are given in Appendix A. The series is $\Lambda_1(x, y) = \sum_{n=0}^{\infty} \frac{y^n}{n!(n-\bar{\gamma})} [x^{n-\bar{\gamma}} - 1]$, unless the improbable case of $\gamma = n$ [66]. The series converges rapidly and may be truncated after a few terms (we use four terms). At the transition from elastic to plastic behavior, $R = 1$ and $\Lambda_1 = 0$. In that case the tooth pressure simplifies to

$$p_t = p_0 + 2mG\bar{\delta} = p_0 + \frac{Y + (\alpha - 1)p_0}{2(m + \alpha)/m}. \quad (26)$$

This limit is both relevant and simple to implement.

2.4 Stress distribution from a load

The stress distribution in a semi-infinite, homogeneous, isotropic elastic medium can be computed analytically in a number of different load cases. The solution for a point load was first derived by Boussinesq. The vertical stress at a depth z under a uniform load, σ_s , distributed over a circular area A_s is given by

$$\sigma_z^v(z, \sigma_s, A_s) = \sigma_s \left[1 - \left(\frac{z}{\sqrt{A_s + z^2}} \right)^3 \right]. \quad (27)$$

2.5 Variable soil compaction

The mass density and material strength of a soil depends on its state of compaction, moisture content and pore pressure. The nominal state of a soil is also referred to as the *bank state*. This refer to a particular bulk mass density ρ_b , confining stress σ_b and strength parameters ϕ_b , c_b , etc. The bank stress is usually taken as $\sigma_b = 1$ kPa. If the confining stress is increased to $\sigma > \sigma_b$ the soil might compact such that $\rho > \rho_b$. There are several equivalent ways to represent a state of compaction, e.g., the *void ratio* $e = V_v/V_s$, *porosity* V_v/V or *volume fraction* $\varphi = V_s/V$, where V_v is the (internal) void volume, V_s is the volume of solid particles and $V = V_v + V_s$ is the total volume. An alternative measure of compaction is the bulk mass density relative to the bank state $\rho/\rho_b = V_b/V$, where V_b is the volume that the soil occupied in its bank state. For most soil, the shear strength and stiffness increase with the level of compaction. When soil material is mobilized and subject to shearing, e.g., being excavated or otherwise energized to flow, it expands in volume and become looser and ρ decreases. Usually, the shear strength and the stiffness decrease when the material become looser.

Mass *swelling* is simply a state of compaction where the mass density is less than the nominal value for the material. This may occur if the soil is disturbed into a shear flow. The *swell factor* is defined $S = V/V_b$ such that $\rho = S^{-1}\rho_b$. It ranges from 10-40% for most soils [8]². For broken rock it can range up to 50-80%.

2.5.1 Compressive strength

The compressive strength is usually characterized using the *compression index* [58, 11]

$$C_c \equiv \frac{e_b - e}{\ln(\sigma/\sigma_b)} \quad (28)$$

Many material show the logarithmic dependency between compaction and stress expressed by Eq. (28). When the compression index is measured relative to the bank state it is known as the *Virgin compression curve* (VCC). A typical range of compression index is from 0.01 to 10. Loose packed sand has compression index between 0.05 to 0.06 in the load range from 100 kPa to 4 MPa, while dense packed sand has compression index between 0.02 to 0.03³. The compression index for clay range from 0.2 to 5, the latter ones with organic content. Peat may have compression index around 10. It is important not to confuse the compression index with the *compression constant*⁴ Also, the compression index is many times defined in terms of the base-10 logarithm instead of the natural logarithm. The two compression index values differs then by a factor 2.3.

²https://www.engineeringtoolbox.com/soil-rock-bulking-factor-d_1557.html

³<https://www.finesoftware.eu/help/geo5/en/compression-index-01/>

⁴The state of compaction and compressive strength may also be measured in terms of the volumetric strain $\varepsilon = \text{tr}\bar{\varepsilon}$ and a *compression constant* \bar{C}_c with the relation $\varepsilon = -\bar{C}_c^{-1} \ln(\sigma/\sigma_b)$. The compression constant is related to the compression index by $\bar{C}_c^{-1} = C_c/(1 + e)$.

Note the identity $e + 1 = (V_v + V_s)/V_s = V/V_s = \rho_s/\rho$, with the particle mass density ρ_s . Consequently $e_b - e = \rho_s(\rho - \rho_b)/\rho_b\rho$ and hence⁵

$$\rho = \rho_b \left[1 - \varphi_b C_c \ln \left(\frac{\sigma}{\sigma_b} \right) \right]^{-1} \quad (29)$$

where the relation for the volume fraction $\varphi = (1 + e)^{-1} = \rho/\rho_s$ is used.

2.5.2 The effect of compaction on stiffness and shear strength

The state of compaction influences the stiffness and shear strength and of a soil. These phenomena are covered by the *critical-state theories*, which extends conventional elastoplasticity to include the compaction state as an internal variable. The most renowned model is the Cam-Clay model [3].

To understand how the bulk elasticity depends on the compaction, start by considering to contacting spherical bodies obeying the Hertz contact law $f = k\delta^{3/2}$, with overlap δ , normal stiffness $k = E^*\sqrt{2d}/3$ in terms of the effective Young's modulus $E^* = E/2(1 - \nu)$ and the particle diameter d . In terms of stress $\sigma = f/d^2$ and strain $\varepsilon_{1D} = \delta/d$ this reads $\sigma = (\sqrt{2}/3)E^*\varepsilon^{3/2}$. By definition, the 1D bulk modulus become $K_{1D} = \partial\sigma/\partial\varepsilon = (3/\sqrt{2})E^*\varepsilon_{1D}^{1/2}$. Observe that the bulk stiffness is not constant but depend on the compression as $\varepsilon^{1/2} = \eta^{-1/2}$. This generalizes to higher dimensions of granular packings [3] $K_{3D} = ZE\sqrt{\Delta V/V}$, where K_{3D}^0 is the bulk stiffness at a reference state (bank state) and Z is the average number of contacts per grain, which may increase with compaction, i.e. $Z(\Delta V/V)$. This suggest that the bulk effective Young's modulus scale as

$$E_{\text{bulk}} = E_{\text{bulk}}^0 \left[1 \pm k_E \left| \frac{\rho}{\rho_b} - 1 \right|^{n_E} \right] \quad (30)$$

where we have used $\Delta V/V = \rho/\rho_b - 1$, E_{bulk}^0 is the bulk elasticity at bank state, and k_E and n_E are hardening parameters that for an ideal packing with constant Z have value 1 and 0.5, respectively. The sign depends on compaction versus expansion. Note that relative density ρ/ρ_b may be substituted for the relative volume fraction φ_b/φ .

Compacted material experience larger dilatancy, expansion when shearing. The dilatancy add to the internal friction such that the (non-cohesive) Mohr-Coulomb law modifies to $\tau = \mu(\phi, \psi)\sigma$ [3, 65], with

$$\mu = \tan(\phi + \psi) \quad (31)$$

and internal friction angle ϕ and dilatancy angle ψ . Roux and Radjai [47] proposed

$$\psi = c_\varphi(\varphi - \varphi_c) = c_\rho \left[\frac{\rho}{\rho_b} - \frac{\rho_c}{\rho_b} \right] \quad (32)$$

for some constant c_φ and c_ρ , and φ_c and ρ_c is the critical packing fraction and density, respectively, where the soil switch between positive dilation (volume expansion) and negative dilation (volume shrinkage) upon shearing. If the dilatancy is given in bank state, the constant c_ρ can be determined from $\psi_b = c_\rho[1 - \rho_c/\rho_b]$.

2.6 Previous work on terrain simulation models

The first physics-based models for real-time simulation of heavy equipment and deformable terrain appeared in the literature around 2000. Park [41] developed an elaborate model for the digging resistance in soil for the purpose of construction excavator VR simulators. The model extends the fundamental earthmoving equation from a blade (separating plate) cutting a horisontal soil bed to digging in sloped terrain with a bucket. The shape of the

⁵This differs from the expression in [33], i.e., their C is not a dimensionless compression index.

failure zone is approximated as a wedge. Park’s model include also penetration resistance and the idea that deadload material in the bucket forms an effective secondary separation plate.

The solution in Vortex from CM Labs Simulations combines the fundamental earthmoving equation (FEE) with particle dynamics to model the cutting resistance and motion of the soil [17]. Static soil, represented in a 3D grid, is adaptively converted into particles. The portion of the terrain in front of the tool which has not yet undergone failure provide resistance, limited by the FEE, and using the method of trial wedges. The extension by [32] to sloped terrain is used for predicting the soil wedges. The particles exchange contact forces with the tool and add weight (surcharge) the FEE. Two wheel-terrain interaction models are implemented, the semi-empirical Bekker-Wong model [64] and model where the stress in the contact interface is estimated using elasto-plasticity theory [4]. Also Mevea’s solution [20] combine a grid and particle-based representation of the soil. Vertical contact forces cause soil compression and displacement using a cellular automata. Horizontal contact forces generates particles if the force is greater than some undisclosed *shear impulse limit*.

Based on Bekker-Wong-Reece theory, Krenn and Hirzinger [27] developed the semi-empirical *soil contact model* (SCM) for multi-body simulations of planetary rovers. The model has been extended and evaluated for performance in [9], and it has been implemented in the Chrono Engine [55]. The model appear suitable for realtime simulation but limited slowly moving vehicles, given the basic assumptions leading to the model. A similar model for predicting the sub-soil stress and resulting deformation from detailed geometric representation the tire and terrain interface was developed by Madsen [33].

The meshfree elastoplastic terrain model developed by Nordberg and Servin [39] was intended for realtime simulation including contacting multibody systems. It remains unknown what performance can be achieved with an iterative solver at the necessary resolution and mass ratios.

3 agxTerrain

3.1 Outline of the agxTerrain model

The `agxTerrain` is a multiscale model of terrain dynamics that combines standard continuum soil mechanics with particle and rigid multibody dynamics. An adaptive model order reduction (AMOR) technique provides automatic transformation between the different levels of abstraction of the local terrain in the vicinity of a machine’s tool or ground contact elements. Fig. 4 illustrate the main ideas.

The deformable solid is discretised in a regular grid of *voxels* that is assigned field variables, including mass density, compaction, velocity etc. The boundary voxels, where the mass density drop to zero, define a *surface heightfield* that is used for modeling contacts with a machine or other objects. The contact forces on the surface imply a stress field in the terrain that may cause soil compaction. A body that has the property of being a *deformer* or a *digging tool*⁶ may also cause localized shear failure, i.e., soil cutting or displacement.

A digging tool is equipped with a *cutting edge*. A potential failure surface through the soil is predicted when a cutting edge come in contact with a terrain. The shape of the failure surface depends on the geometry of the tool and the terrain surface, and on the local soil parameters. The volumetric region confined by the surface heightfield, contacting object and the failure surface defines an *active zone*. The active zone may fail if in a state of critical stress. The failure is manifested by a shear flow, either localized to the failure surface or distributed over the bulk of the active zone.

The active zone is resolved into particles of variable size. When a cutting edge moves into a resting terrain the solid voxel mass in the active zone is gradually converted to

⁶A digging tool is referred to as a *shovel* in AGX.

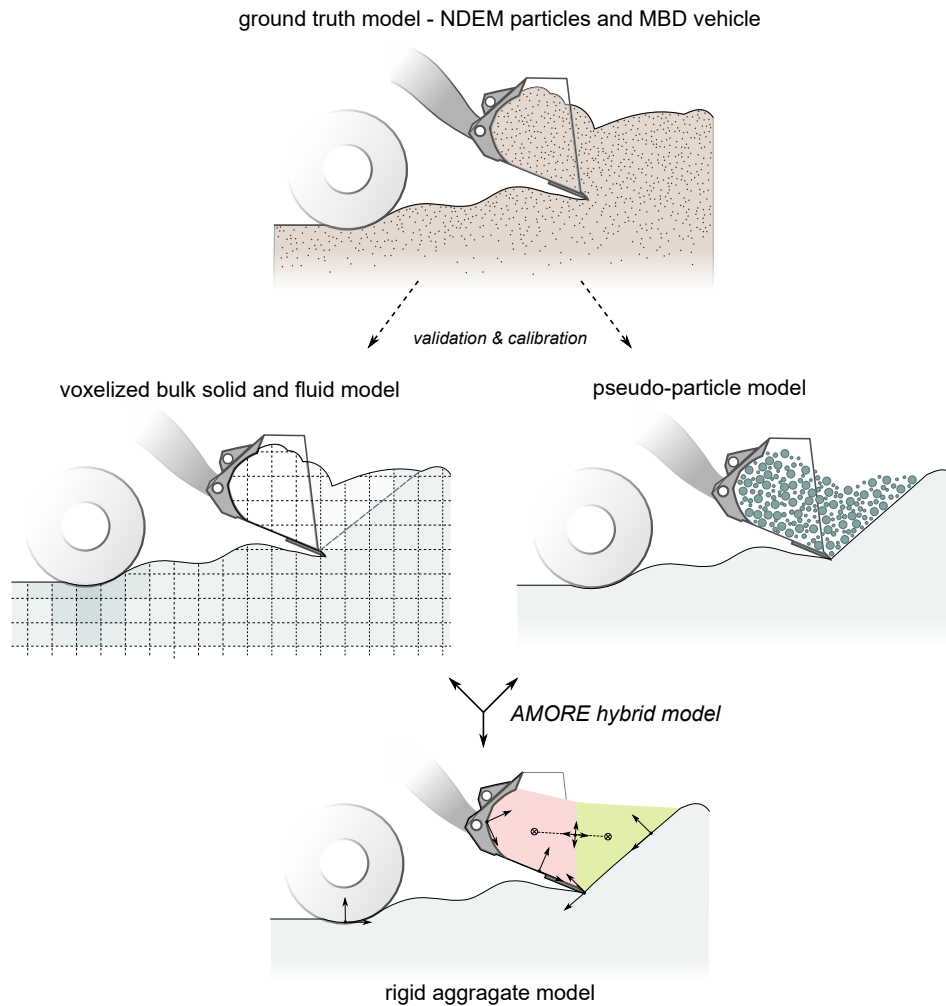


Figure 4: The *agxTerrain* is a multiscale model that combine continuum soil mechanics with particle and rigid multibody dynamics. The mass density, compaction and velocity fields of the soil is represented in discrete form using a regular grid. In the digging tool’s active zone the fluidized mass is resolved using a particle representation. The strong coupling between the tool and the terrain is mediated using a low-dimensional rigid aggregate model for the the soil in the active zone. The key model parameters are the standard bulk parameters of soil dynamics. The model is validated and calibrated using a “ground truth” model with resolved soil dynamics using nonsmooth DEM.

particles by creation of new particles or growth of existing ones. This modifies the surface heightfield to coincide with the failure surface. The conversion is designed to guarantee mass preservation and support soil cutting at high precision.

The particle dynamics of the liberated soil is modelled using the nonsmooth DEM, described in Sec. 2.1.3. Particles may contact with other particles, rigid bodies (tool) and with the variable surface heightfield. The particles inherit their material properties from the solid voxels from where they originate using a mapping between DEM model parameters and the bulk mechanical parameters. The particles experience the contacting tool (rigid body) as a kinematic objects.

The digging tool, and the multibody system it is part of, experience the material inside the active zone as a single dynamic *aggregate body*, which is a pair of rigid bodies connected by a 6 d.o.f. constraint with compliance and force limits that emulate the stiffness and strength of material in the active zone. The centre of mass position, velocity and inertia of the rigid aggregate is continuously updated from the current state of the particle system. The aggregate interacts with the tool body and surface heightfield through contacts with normal, frictional and adhesive forces. The use of the aggregate body as a proxy body for the particles reduce the computational complexity substantially and ensures numerical stability, allowing for large time-step integration and fast simulation.

When the digging tool penetrate the terrain surface it experiences also a penetration resistance force in addition to the separation force and inertia of the aggregate body.

Particles that come to rest outside the active zone are converted back to solid terrain, with the entire mass distributed over adjacent voxels respecting the maximum angle of repose for the soil. Each voxel has a maximum solid occupancy (mass content) that corresponds to the maximum bulk density of the soil.

The stiffness and strength of the solid terrain depend on the local state of compaction, which in turn depend on the presence of external loads on the surface heightfield causing subsoil stresses.

The key model parameters for either level of abstractions are the standard soil parameters. Values for these may be found in literature, or be identified and calibrated from physical experiments directly, or via “ground truth” simulations of a reference model composed of high-resolution particle system and rigid multibody system. Additional model parameters are the geometry of the tool or ground contact elements, such as the *cutting edge* and *teeth*. The compliance and strength of the aggregate body have default values that may be calibrated also guided by NDEM “ground truth” simulations.

3.1.1 Main algorithm

The agxTerrain operates according to the following algorithm:

1. Initialize the terrain.
 - (a) Assign mass distribution and bank state properties to voxels
 - (b) Apply terrain equilibration for a soil-consistent initial state
 - (c) Update surface heightfield
2. Initialize a machine with a tool
 - (a) Define contact material for objects and terrain surface
 - (b) For digging tool and deformer, define edges and direction vectors
3. For each simulation time-step
 - (a) Pre-collide update of the solid terrain
 - i. Predict active zones for deformers and cutting edges intersecting the terrain
 - ii. Convert voxel mass in the active zone into particles and fluidized mass
 - iii. Merge resting particles at safe distance outside active zone into voxel mass
 - iv. Apply terrain equilibration for a soil-consistent terrain state
 - v. Update the surface heightfield
 - (b) Collision detection
 - (c) Generate aggregates
 - i. Compute the voxel and particle mass distribution in each active zone
 - ii. Create aggregates, discretised in rigid body pairs locked together
 - iii. Define minimal set of contacts between aggregate, tool and terrain surface
 - (d) Penetration force
 - i. Estimate the pressure force on the digging tool face and cutting edge
 - ii. Compute penetration force limits
 - iii. Set a tool-terrain penetration constraint
 - (e) Solve the coupled dynamics
 - i. Direct pre-solve for machine-tool-aggregate-terrain surface
 - ii. Iterative solve for soil particle dynamics and loose objects
 - iii. Direct post-solve for machine-tool-aggregate-terrain surface
 - (f) Position update
 - (g) Post-solve update of the solid terrain
 - i. Compute the sub-soil stress field from the surface contact forces
 - ii. Predict soil compaction and redistribute voxel mass vertically
 - iii. Update the soil strength parameters

3.2 Assumptions and delimitations

The agxTerrain model rests on a number of simplifying assumptions. If these assumptions are significantly violated the behaviour of the simulation model may deviate from the real system.

The terrain is assumed nearly homogeneous and isotropic on the length-scale of machine tool, or contact elements, and down to spatial dimensions of the true grain size. The soil is assumed not to contain coarse rocks or roots unless modelled explicitly. Moisture content is assumed constant and homogenous and is therefore not modelled explicitly but only indirectly by its effect on soil friction and cohesion. Variable temperature is not taken into consideration.

The terrain is further assumed to be a multiphase solid with an elastoplastic phase and a fluent phase. In the elastoplastic phase the deformations are assumed to be quasistatic,

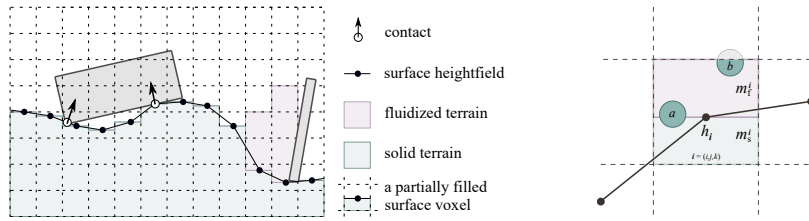


Figure 5: Illustration of the voxelized representation of the terrain and the surface heightfield (left) that intersect the surface voxels at a position that depend on the solid occupancy of the surface voxels (right).

with shear strength according to a Mohr-Coulomb law and a plastic compression law that are independent of strain rate. Inertia effects are assumed negligible. In the fluent phase the soil is assumed to be a frictional and highly dissipative granular media. Inertia effects are assumed significant except in regions where the soil is very dilute, an assumption that is not valid for the motion of the soil but for its effect on the surroundings.

It is assumed that the part of the terrain that is in dense solid phase has an upper boundary that define a single-valued function, a *surface heightfield* function $z = h(x, y)$.

3.3 Model components

The different components of the `agxTerrain` model are described in more technical detail below.

3.3.1 Solid and fluidized terrain

The soil is regarded as a two-phase media with mass density, compaction and velocity as fundamental state variables. A set of *soil parameters* describe the physical properties of the soil in its nominal *bank state*. The bank state soil parameters include mass density ρ_b , internal friction angle ϕ_b , cohesion c_b , dilatancy angle ψ_b , bulk elasticity modulus E_b . These are collected in a bulk parameter vector

$$\mathbf{p}_b = \begin{bmatrix} \rho_b \\ \phi_b \\ c_b \\ \psi_b \\ E_b \end{bmatrix}. \quad (33)$$

The mass density, $\rho(\mathbf{x}, t) = \rho_s(\mathbf{x}) + \rho_f(\mathbf{x}, t)$, is composed by the solid mass density, ρ_s , and fluidized mass density, ρ_f . The mass distribution is discretised with a regular cubic grid. Each grid cell, or *voxel*, has an index triplet $\mathbf{i} = (i, j, k)$, center point $\mathbf{x}_i = [x_i, y_i, z_i]$ and volume $V_0 = l_0^3$. The solid mass density has a natural bank state value ρ_b , but can vary in each voxel $\rho_s^i \in [\rho_{\min}, \rho_{\max}]$. We define solid *mass compaction* as $w_i = \rho_s^i / \rho_b$. All voxels except surface voxels are assumed to be fully occupied with solid mass of density ρ_s^i . Surface voxels may be partially filled with solid mass of density ρ_s^i occupying a volume $V_s^i \leq V_0$. We define *solid occupancy* by $\varphi_i = V_s^i / V_0 \in [0, 1]$. When the voxel is maximally filled with solid mass the solid fraction is $\varphi^i = 1$. When it is not filled, there is a volume of void V_v^i (additional to any void embedded in the solid mass at particle level) such that $V_0 = V_s^i + V_v^i$. See Fig. 5 for an illustration. The amount of solid mass in a voxel i is consequently $m_s^i = \rho_s^i V_s^i$. The dynamic state vector for each voxel thus become

$$\mathbf{s}_i = \begin{bmatrix} m_s^i \\ w_i \\ \varphi_i \\ \mathbf{u}_i \end{bmatrix}. \quad (34)$$

A change in compaction affects the local mass density and soil strength, that is, the local soil parameters are functions of the voxel's state vector and of the bank state parameters, i.e., $\mathbf{p}_{bi}(\mathbf{s}_i, \mathbf{p}_b)$. The time evolution of $\mathbf{s}_i(t)$ is ensured by a set of transition rules in combination with transformation into and from particles and fluidized mass. These are constructed to preserve mass and momentum, and model a dynamical system consistent with the prescribed law of elastoplasticity and material parameters ⁷.

A voxel may contain both solid and fluidized mass. Fluidized mass is assumed to be in a gaseous state, loosely packed and lacking bearing capacity. Only voxels with no solid mass or partially filled surface voxels may contain fluidized mass. Fluidized mass is considered a temporary matter state, soon to be converted into particle mass or solid voxel mass. During its short-lived existence, fluidized mass can fall to the ground or be advected with the local mass flow of particles and solid terrain. Fluidized mass is a buffer that is needed to ensure total mass conservation while avoiding unphysical states of compaction. The alternative is to introduce more and smaller particles, but this would dramatically affect the calculation time. Currently the motion of the fluidized mass is rule-based rather than computed from a momentum balance equation. Therefore, situations should be avoided where the fluidized mass dominates over the solid mass or particle mass.

The voxel data representations and operations are implemented using the *Open VDB*⁸ library [37]. It is optimized for large, sparse, time-varying volumetric data discretised on a 3D grid and support hierarchical representations.

3.3.2 Terrain surface heightfield

A surface heightfield $z = h(x, y)$ is assigned to the terrain. It has the role of collision geometry with other objects and for visualization of the current shape of the terrain. It has a discrete representation $h_{ij} = h(x_i, y_j)$. The height value in a column (i, j) is the centre position, $z_{i'}$ of the top-most non-empty voxel, $\mathbf{i}' = (i, j, k')$, plus the local mass fill ratio relative to that voxel centre, i.e.,

$$h_{ij} = z_{i'} + (\varphi_{i'} - 1/2)l_0, \quad (35)$$

Note that this make the surface heightfield a continuous function of the solid occupancy. Between the grid points the surface height field is interpolated linearly. See Fig. 5 for an illustration.

3.3.3 Subsoil stress from surface contacts

Surface contacts are grouped into contact patches with total normal force f_s . Each contact patch cover a certain surface area, A_s , equal to the sum surface voxel areas A_s^j inside the patch. The normal stress is assumed evenly distributed over the contact patch, i.e., $\sigma_s^j = f_s/A_s$. The subsoil stress in a voxel \mathbf{i} at depth z_i and straight under \mathbf{i} is computed as $\sigma_i(z_i, \sigma_s^j, A_s^j)$ using Eq. (27). This is illustrated in Fig. 6.

3.3.4 Soil compaction

The model for soil compaction described in Sec. 2.5.1 is assumed. The local state of compaction in a voxel i is determined by Eq. (29) to

$$w_i = \frac{\rho_i}{\rho_b} = \left[1 - \varphi_b C_c \ln \left(\frac{\sigma_i}{\sigma_b} \right) \right]^{-1} \quad (36)$$

⁷The model architecture and data structures are prepared for a representation of multidimensional fields of displacement, velocity, strain and stress, but currently there is no supported implementation for elastodynamics, or for plastic or viscous flow based on numerical time-integration of the time evolution equations (15) and (16).

⁸<https://www.openvdb.org>

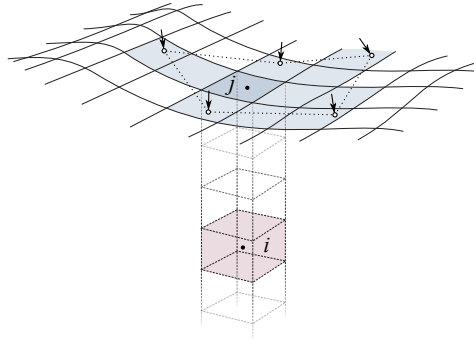


Figure 6: The contact forces (vectors) lead to a normal surface stress on a contact patch (blue) from which the subsoil stress in a voxel i (pink) is estimated. If a voxel is compacted the corresponding amount of soil mass is propagated vertically from voxels above leading to a sinking heightfield surface.

where σ_i is the estimated stress in voxel i . The compaction is clamped to a state of maximum mass density ρ_{mass} and the stress propagation is truncated at a depth where it is smaller than a given threshold σ_{min} .

When compaction occur, soil mass is propagated vertically to fulfil the condition that all solid mass voxels, except surface voxels, have unit solid occupancy. The surface heightfield will move downwards as a consequence of the soil compaction.

The local soil parameters are updated from the local state of compaction using the formulas in Sec. 2.5.2. The dilatancy angle is computed

$$\psi_i = c_\rho [w_i - w_c] \quad (37)$$

The internal friction become $\mu_i = \tan \phi_i$ with *effective angle of internal friction*

$$\phi_i = \phi_b + \psi_i \quad (38)$$

The critical mass compaction w_c^{-1} is usually not known. If it is set to $w_c = 1$ the soil is non-dilatant at bank state. If it is set to $w_c = \rho_{\text{min}}/\rho_b$ the soil will always be dilatant. The elastic modulus is computed

$$E_{\text{bulk}}^i = E_{\text{bulk}}^0 [1 \pm k_E |w_i - 1|^{n_E}] \quad (39)$$

with hardening parameters k_E and n_E and the sign depending on compaction or expansion.

Soil compaction is considered to be a plastic deformation. The compacted state is permanent until the soil is disturbed with a new load or put into shear flow e.g. by excavation. The same holds the altered soil stiffness and strength.

3.3.5 Terrain equilibration

A soil has a maximum angle of repose δ_b . For simplicity we identify the angle of repose of a soil with the effective internal friction angle, given by Eq. (38). Beyond this slope the terrain is not in a stable equilibrium and would fail and avalanche into a valid state if it is transformed into pseudo-particles. *Terrain equilibration* is an algorithm that searches the voxelized terrain for local slopes that exceed the angle of repose and perform a local mass distribution in the steepest direction. The algorithm is an iterative process, a *cellular automata* [43], that terminates when the terrain is in a valid equilibrium state. The algorithm can be limited to a maximum change in solid occupancy per time-step, which is equivalent to a maximum flow rate. The resulting terrain equilibration correspond to an avalanche flow that occur either instantaneously or gradually. This is applied automatically

at each simulation time-step. It is recommended to apply terrain equilibration when a new terrain is created or modified by direct operation on the solid voxel mass distribution or soil parameters.

3.3.6 Digging tool

A *digging tool* is equipped with a *cutting edge* and a *top edge*. These are assumed to be parallel. A digging tool is also assigned a *penetration direction* orthogonal to the cutting edge. See Fig. 7 for an illustration. This enables soil penetration and cutting. If the digging tool is not a flat blade, but of concave shape, the penetration direction implicitly indicate a *primary separation plate* and an *inner shape* that is the void enclosed by the cutting edge, top edge and the concave tool surface connecting them. When a cutting edge overlap with nonempty voxels an active zone (section 3.3.8) is predicted. The digging tool will experience the resistance of an aggregate body (section 3.3.13), that represent the soil mass inside the active zone with frictional cohesive contacts with the tool and the terrain.

A digging tool also experience a *penetration force* on the primary separation plate and cutting edge. If the digging tool has teeth at the cutting edge, this can be accounted for in the penetration force model. The model takes the number of teeth, and their diameter at the tip and at the base, as input. The penetration resistance force is modeled with a velocity constraint $\mathbf{t}_p^T \mathbf{v}_e = 0$. This produce a constraint force, f_p , hindering any motion of the tool with the cutting edge velocity \mathbf{v}_e in the penetration direction \mathbf{t}_p . The constraint force is given an upper and lower limit⁹

$$f_{p,\min} \leq f_p \leq f_{p,\max} \quad , \quad \text{where} \quad \begin{aligned} f_{p,\min} &= -f_{ps}(p_n) \\ f_{p,\max} &= f_{ps}(p_n) + f_{pt}(p_t) \end{aligned} \quad . \quad (40)$$

Only if the constraint force reaches this limit will the tool be able to move in the penetration direction. The penetration resistance of the separating plate, $f_{ps}(p_n) = (c_a + p_n \mu_{\text{tool}}) A_s$, and of the teeth, $f_{pt}(p_t) = f_{pt} = n_t [p_t + (c_a + p_t \mu_{\text{tool}}) / \tan \alpha] A_t$, are described in Sec. 2.3.3. The normal pressure, p_n , is computed by Eq. (22), taking the lateral earth pressure and tool inclination into account. The tooth pressure is modelled by the cavity expansion theory, and we use the pressure at the elastic to plastic transition in Eq. (26). A digging tool with no teeth is modelled as a tool with a single teeth, i.e., $n_t = 1$.

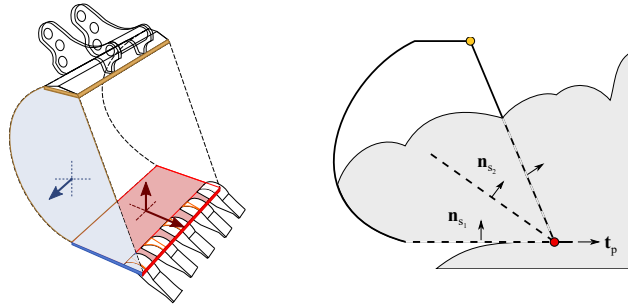


Figure 7: The left image illustrate a digging tool with a cutting edge (red line), separating plate (red face), deformer edge (blue line), deformer face (blue face) and top edges (yellow line). The inner shape is indicated with the dashed lines. The penetration direction, separation normal and deformation normal vectors are indicated. The right image illustrates the formation of a secondary separation plate, moving from the original separation plate (ground plate) to the plane that connects the cutting edge and top edge as the bucket fill ratio increase.

As the digging tool is filled with material this forms a dead load that acts as a *secondary separation plate*. When the digging tool is entirely full, the secondary separation plate is

⁹Up to version AGX 2.27, the lower limit is $f_{p,\min} = -f_{ps}(p_n) - f_{pt}(p_t)$.

defined by the plane connecting the cutting edge and the top edge. When it is empty the separation plate is set by the ground plate (penetration direction). When the digging tool is partially filled, the inclination of the separation is a continuous interpolation between these limits. The model contains a parameter¹⁰ for what fraction of the bucket fill ratio the secondary separation plate is fully developed. This make the transition of the separation plate to secondary separation smooth. The orientation of the separation plate is used to compute the size and shape of the active zone, which in turn affect the digging tool reaction force. No particles contact directly with the secondary separation plate.

A digging tool with side walls, such as the bucket in Fig. 7, can be equipped with pairs of *deformation edges* and parallel *top edges*. This enables soil displacement in the direction of the deformation normal. This part of the digging tool then acts as a soil deformer, which is explained in the following section.

3.3.7 Soil deformer

A *soil deformer* is an object that interact with the terrain trough pushing soil instead of cutting soil. A soil deformer can be assigned one or several pairs of *deformation edges* and parallel *top edges*. The pairs define separation plates which can displace soil and experience resistance force. A deformation edge and face has no inner shape, no secondary separation plate and no additional penetration resistance to that of the aggregate. The shape of the deformer surface is assumed flat or concave and is given a normal orthogonal to the defining edges. An example of box-shaped deformer is shown in in Fig. 8. Similar to a cutting edge, a deformation edge that overlap with nonempty voxels indicate an active zone that liberate solid mass into fluidized, forming particles and an aggregate body that resist the motion of the deformer thanks to frictional cohesive contacts with the tool and the terrain.

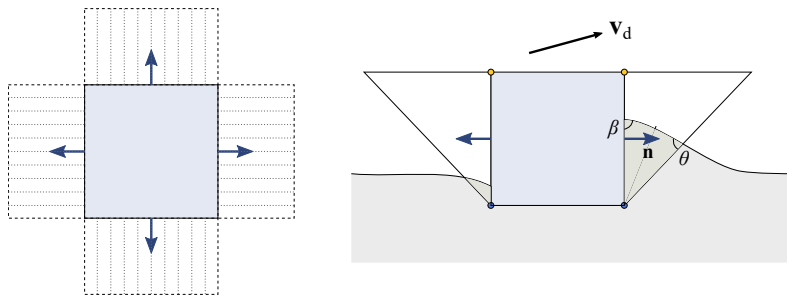


Figure 8: Illustration of a box-shaped soil deformer with deformation edges (blue) and top edges (yellow). The active zones define aggregates that provide resistance. The soil material inside the active zones is not converted into particles but is displaced directly using the resulting velocity of the body projected on the respective face normal.

3.3.8 Active zone

The active zone is approximated by a wedge (several actually), similar to as described in Sec. 5.1, and we propose a generalization to sloped terrain that differs from Park's model in Eq. (20). In the proposed model, motivated by DEM simulations and illustrated in Fig. 9, the angle between failure plane and the terrain surface is

$$\theta(\phi, \beta) = \frac{\pi}{2} - \left(\frac{\phi + \beta}{2} \right), \quad (41)$$

where β is the angle between the tool and the terrain surface and ϕ is the mass weighted average of the local internal friction angles ϕ_i in the active zone. The angle θ between

¹⁰SecondarySeparationDeadloadLimit

failure plane and the terrain surface is also an average found after a uniform of the wedge along the cutting edge and an averaging search along each vertical segment.

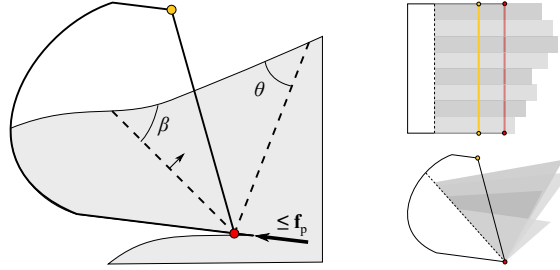


Figure 9: Illustration of the wedge base active zone model with the effective separation plate and failure surface indicated.

A general terrain surface is not plane. Therefore the shape of active zone is not approximated by a single wedge, but discretised along the cutting edge (or deformer edge) by a number of vertically aligned wedges, as illustrated in Fig. 8 and 9. For each soil wedge, an individual failure angle is computed based on the local tool-terrain inclination and internal friction. Consequently, the shape of the failure zone can vary along the cutting edge (or deformer edge). This allows for realistic soil-tool interaction in terrain with complex shape.

3.3.9 Conversion from solid mass

When a cutting edge moves into voxels with solid mass, a failure surface is predicted and the mass inside the active zone is converted into particles or fluidized mass. Voxels that are partially inside the active zone are only partially converted into particle or fluidized mass such that the resulting surface heightfield coincide with the failure surface. This is illustrated in Fig. 10. The to-be-converted solid mass can produce new particles or be accumulated by already existing particles that grow correspondingly. The conversion is local to the voxel or its neighbours. The size of the particles range between a minimum and maximum size. There may be insufficient space for conversion into particle mass. That lead to residual mass that is converted into fluidized mass.

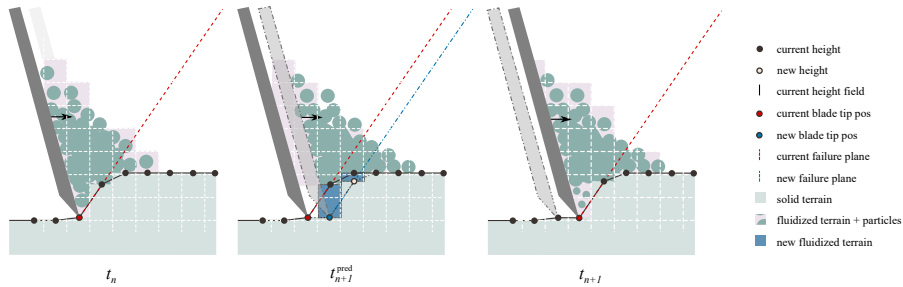


Figure 10: As a blade and its active zone moves into the terrain, new solid voxels are resolved into particles or fluidized mass that form the aggregate body. The voxel height value, corresponding to the solid occupancy, is found by projection to the failure plane of the active zone.

3.3.10 Particle creation, growth and mass exchange

The change in solid occupancy means a corresponding change in solid mass. This change is converted first into fluidized mass and next into particle mass, either by creating new particles or by adding to existing particles that consequently grow in size given the fix particle mass density. Mass may also be exchanged between particles. The particle size is

restricted by a minimal and maximal size, $d \in [d_{\min}, d_{\max}]$, growth of the smallest particles are favoured and there is a maximum growth rate, $\dot{d} \leq \dot{d}_{\max}$. The mass exchange is limited to occur in bins of size $3 \times 3 \times 3$ voxels. By construction, all mass exchange operations preserve the total mass and respect the mass continuity equation locally.

If not all liberated solid mass in a voxel can be converted into particle mass it remains *as residual fluidized mass*. Any fluidized mass found outside the active zone is projected vertically onto the heightfield surface, where it is converted back into solid mass. Inside the active zone the fluidized mass is transported with the local particle velocity. If the fluidized mass density is found to exceed the maximum value ρ_b , the excess fluidized mass is simply propagated upwards (opposite the direction of gravity) to vacant voxels.

3.3.11 Conversion from particles into solid mass

Particles that come to rest on the terrain outside an active zone are converted back to solid voxel mass. The conversion condition includes thresholds on the contact velocity, distance to nearest active zone and a delay time for meeting these conditions. A swell factor is applied to the soil that is converted from particles into solid voxel mass. The stiffness and strength of the swollen voxel mass is computed as in Sec. 3.3.4. After conversion into solid voxel mass the terrain is equilibrated as described in Sec. 3.3.5.

If there is a gap between the cutting edge to the terrain heightfield surface, the particles in the vicinity will decay gradually by losing part of its mass to the solid terrain until the gap is filled. This enables high-resolution grading even when the gap is smaller than the particles. This is illustrated in Fig. 11 and 12.

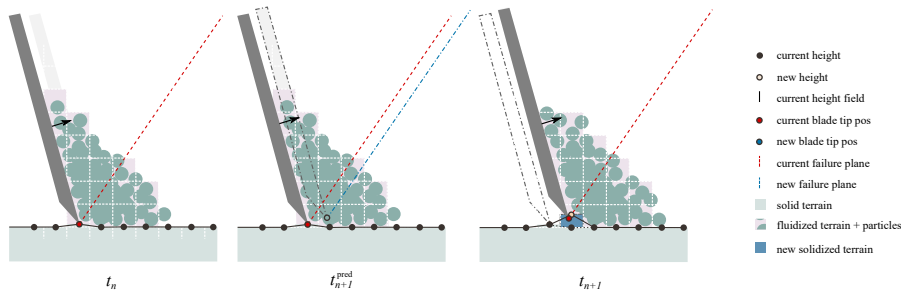


Figure 11: A raising blade causing a gap between the cutting edge and the terrain, that is filled by conversion of particle or fluidized mass.

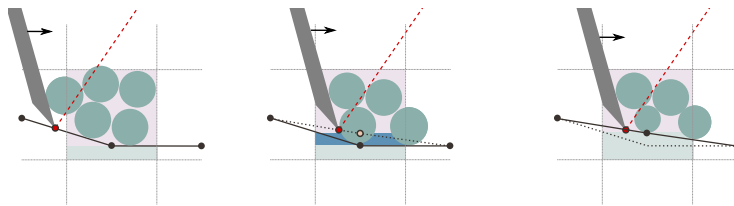


Figure 12: Higher detail of a raising blade filling of the gap by conversion of particle or fluidized mass.

3.3.12 Soil particles

Mass inside the active zone is converted into a *pseudo-particle* representation of the soil. That means that the particles do not represent the true grains with their actual distribution of size, shape and mechanical properties. Instead, the soil is represented by a collection of large spherical particles with contact parameters - elasticity, friction, cohesion and rolling

resistance - that are calibrated to produce a bulk material with the very same mechanical properties assigned that is to the terrain, e.g., internal friction and bulk cohesion. The particle parameter vector is

$$\mathbf{p}_p = \begin{bmatrix} \rho_p \\ \mu_t \\ \mu_r \\ c_p \\ E_p \end{bmatrix}. \quad (42)$$

The pseudo-particles are simulated using NDEM with a PGS solver (section 2.1.3) in a co-simulation fashion, where the particle system experience the surface heightfield, digging tool and machine as kinematic bodies with collision shapes. The particle simulation time-step is set equal the main simulation time-step. The number of PGS solver iterations is kept as low as possible, e.g., $N_{it} = 25$. This is possible thanks to the aggregate body mediating the strongly coupling between the tool, machine and terrain surface.

3.3.13 Aggregate bodies

The pseudo-particle and fluidized mass inside the active zone of a digging tool form an *aggregate body*, see Fig. 4, which is the object the digging tool and machine experience rather than the particles directly. The mass and inertia tensor is computed from the current distribution of particle and fluidized mass. The set of contacts between particles-to-heightfield and particles-to-digging-tool are reduced to a minimal contact set and is assigned to the aggregate body. The contacts are frictional and cohesive. The force situation is thus very similar to the FEE (19) in Sec. (5.1) but allows for dynamics and inertia.

The aggregate is split into two rigid bodies interconnected with a 6 degrees of freedom (d.o.f.) lock constraint. Each of the two bodies inherits the original aggregate's contacts with the soil tool and the surface heightfield, respectively, and possess no additional collision shape. The 6-d.o.f. constraint is given compliance and force limits so that the aggregate can yield at critical stresses. This avoid the aggregate from behaving unnaturally rigid and overestimation of the reaction force on the tool. The splitting has also a stabilizing effect as the constraint filters out any high frequency contact fluctuations by dissipation.

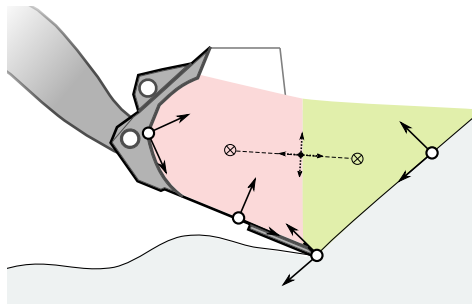


Figure 13: Illustration of a rigid aggregate, that is split in two rigid bodies (pink and green) interconnected with a 6-d.o.f. constraint with compliance and force limits for yielding at critical stress.

4 Parametrization and calibration

4.1 Terrain parameter calibration

The parametrization and calibration of the terrain parameters consist of two steps. The first step is to determine (or choose) the bulk mechanical parameters of the real system that

the simulation model is intended to represent. The second step is to ensure that particle parameters are consistent with the bulk mechanical properties.

There are a number of tests for characterizing soil and calibrate models [64, 10]. The list of tests include uniaxial compression, direct shear [16, 31], annulus shear, triaxial test [10, 54, 5, 40], tilt box [56], cone penetrometer [26, 22], plate test and blade test[40]. The triaxial test is regarded very reliable but is carried out with a material sample put in a testing apparatus and usually in a laboratory environment. The direct shear test is easier to carry out with mobile equipment that can be brought to the field. The cone penetrometer test is ideal for in-situ testing, but the measured cone index do not isolate any specific bulk parameter directly. These three tests are illustrated in Fig. 14 for illustrations of some of the tests.

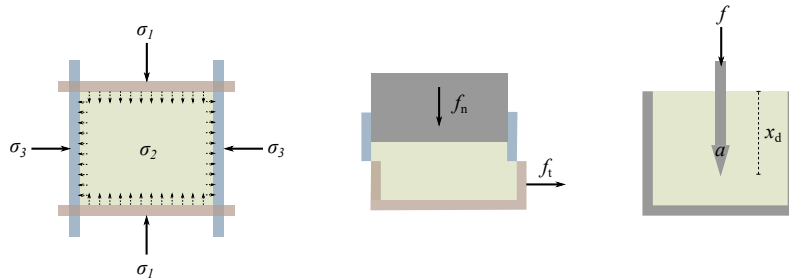


Figure 14: Three common tests for soil parameter identification and calibration are the triaxial test (left), direct shear test (middle) and cone penetrometer (right).

The bulk tests typically provides numeric value to one or more components of the bulk-mechanics soil parameter vector, \mathbf{p}_b , in Eq. (33) that include the mass density, internal friction angle, dilation angle, cohesion, bulk elastic modulus. Additional parameters, such as angle of repose, can also be included. It should be noted that the parameter values typically depend on the packing density (or hydrostatic pressure) at which the test is performed. It is important that the soil sample and test procedure matches the intended bank state. It should also be noted that these values hold for a specific moisture content. If it is not known how these parameters change with moisture it is safest to consider two identical materials, apart from having different moisture content, as two separate materials.

For a given soil bulk parameter vector in the space of possible soils, $\mathbf{p}_b \in \mathcal{P}_b$, it is important that the pseudo-particle parameters have consistent values so that the particle system exhibit the very same bulk mechanical properties. One way of achieving this is to run a series, $n = 1, 2, \dots, N$, of virtual soil characterization experiments, covering a reasonable part of the particle parameter space $\{\mathbf{p}_p^n\}_N \in \mathcal{P}_p$, and measuring the corresponding bulk parameters $\{\mathbf{p}_b^n\}$. The calibrated particle parameters are the one that best fit the bulk properties, i.e.

$$\min_{\mathbf{p}_p^n \in \mathcal{P}_p} |\mathbf{p}_b - \mathbf{p}_b^n|. \quad (43)$$

There is vast literature of characterization of bulk properties of soil. Rather than conducting new experiments it is practical to choose among existing sets of soil parameters, e.g., for sand, gravel, dirt etc. To ease this, a small terrain library is provided in Table 1 with pre-calibrated particle parameters. Having a function for $\mathbf{p}_b = f(\mathbf{p}_p)$, or its inverse $\mathbf{p}_p = f^{-1}(\mathbf{p}_b)$, would be practical and is research in progress. But it appears that the particle parameters do not uniquely define the bulk parameters, see Fig. 18 from [63].

4.2 The direct shear test

The direct shear test consist of three rigid bodies that constitute a shear cell that confine a particle sample. The bodies are a *load body*, *top body* and a *shear body*. The top body

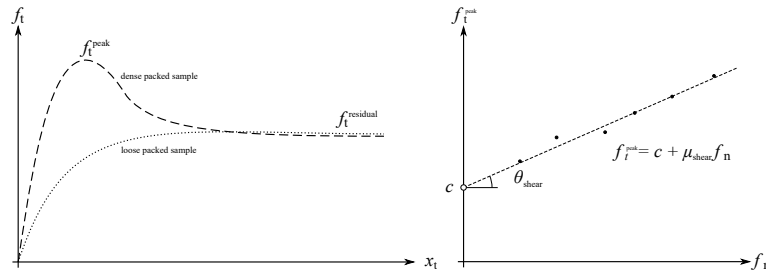


Figure 15: Illustration of the shear force as function of displacement of the shear box for a dense packed material and a loose packed material.

is fix. The load body is free to move vertically. The weight of the load body $f_l = m_l g$ lead to a normal force $f_n(t)$. Because of the dynamics, the normal force is not necessarily constant. The shear body is driven in a direction \mathbf{t} orthogonal to gravity at a controlled speed v_t . The material resists this motion with a tangential shear force $f_t(t)$ that is the particle contact forces onto the shear body projected along \mathbf{t} . If the particle sample is not very loose, the typical behaviour is that $f_t(t)$ increase quickly up to a *peak strength* f_t^{peak} , after which it levels off to a *residual strength* f_t^{residual} , see Fig.15. The *Coulomb internal friction coefficient for direct shear*, at peak strength, is defined

$$\mu_{\text{shear}} = f_t^{\text{peak}} / f_n \quad (44)$$

where f_t is assumed to be measured at stationary equilibrium. This defines a *Coulomb internal shear angle* $\theta_{\text{shear}} = \arctan \mu_{\text{shear}}$. Similar quantities can be computed for the residual shear strength. The Coulomb internal shear angle is different from, but related to, *Mohr the internal friction* μ_b and corresponding angle $\phi_b = \arctan(\mu_b)$ that occur in the Mohr-Coulomb law [3]. The relation to the Coulomb friction angle is

$$\sin \phi_b = \tan \theta_{\text{shear}} = \mu_{\text{shear}} \quad (45)$$

The material sample is first prepared into a state of initial packing. This is achieved by applying hydrostatic compression at a certain stress σ_h . The initial packing determines the shear strength at initial yield ($f_t^{\text{peak}} / f_n^{\text{peak}}$) and dilatancy. The shear strength at stationary shearing ($f_t^{\text{residual}} / f_n^{\text{residual}}$) should however not depend on the initial packing and pressure.

4.3 Triaxial test

The triaxial test is one of the most popular geotechnical laboratory tests for identifying the bulk cohesion, c_b and the internal friction angle, ϕ_b . The bulk elasticity, Poisson's ratio and dilatancy angle can also be identified.

The test procedure can be divided into the two phases of consolidation phase and shear phase. A soil sample is confined between two horizontal plates and surrounded by a cylindrical elastic membrane or four vertical sidewalls. During the consolidation phase the sample is subject to isotropic compression. During the shear phase the vertical plates are driven inward at constant velocity. The lateral stress, $\sigma_2 = \sigma_3$, is held constant. The major stress, σ_1 , and thus also the stress deviator, $\sigma_{\text{dev}} = \sigma_1 - \sigma_3$, is gradually increased to the point where the sample fails and starts shearing indefinitely.

The soil mechanical properties are determined from analysing the stress-strain curves and Mohr circles. Figure 16 shows two typical stress-strain curves obtained from such a test. At *peak strength* the sample fails and starts shearing. The *secant modulus of elasticity*, E_{sec} , is the slope of the secant drawn from the origin through the point of 50% deviator stress at peak strength. Similarly one can identify the *secant Poisson's ratio*, ν_{sec} from the initial soil expansion.

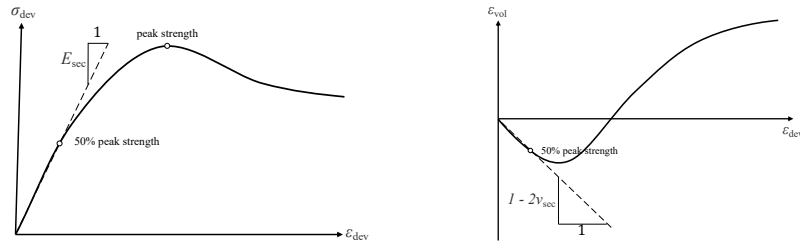


Figure 16: Example of deviator stress and volumetric strain as a function of the deviatoric (axial) strain from a triaxial test. The curves show typical behaviour of for instance dense, dry sand.

The soil strength parameters are determined by performing several triaxial tests with different confining pressures, construct the Mohr circles and the Mohr-Coulomb failure envelope to identify the shear strength parameters, c_b and ϕ_b .

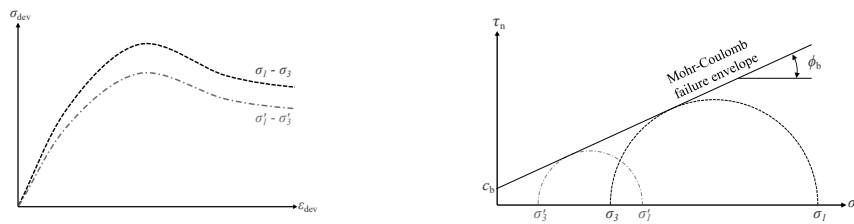


Figure 17: Example of typical stress-strain curves and corresponding Mohr-circles and the Mohr-Coulomb failure envelope. The circles diameters equal to the peak strength deviator stress.

4.4 Terrain library

The terrain library presented in Table 1 has been developed using the direct shear test and triaxial test for mapping the particle parameters to bulk mechanical parameters, see Appendix B and [63]. The shear tests are consolidation to 1 kPa and the triaxial test to 10 kPa, creating initial packings that are close to incompressible. The tangential particle cohesion is an experimental feature and currently not accessible in the main release of AGX Dynamcis or agxTerrain .

Table 1: Relation between particle and bulk parameters using a direct shear test or a triaxial test (gray rows, from [63]).

Name	μ_t	μ_r	c_{pn}	c_{pt}	E_p	ϕ_b	μ_{shear}	c_b
Gravel-1	0.4	0.3	0	0	0.1	37°	0.60	2
Sand-1	0.3	0.1	0	0	0.1	29°	0.49	1
Sand-2	0.6	0.1	0	0	0.1	33°	54	2
Wet-sand-1	0.3	0.1	3	0	0.1	26°	0.44	4
Dirt-1	0.4	0.1	2.5	0	0.1	23°	0.38	3
Dirt-2	0.4	0.1	12.7	0	0.1	29°	0.48	17
Dirt-3	0.4	0.1	63.7	0	0.1	31°	0.51	51
Dirt-soft-1	0.4	0.1	2.5	0	0.01	21°	0.36	4
Clay-1	0.15	0.025	2.5	0.5	0.1	41°	0.65	112
Clay-2	0.06	0.01	2.5	0.5	0.1	39°	0.62	106
FS-strong	0.5	0.1	0	0	0.1	44°	0.69	0
FS-weak	0.3	0.05	0	0	0.1	25°	0.42	0
CFS-strong	0.3	0.05	23	0	0.1	34°	0.56	12
CFS-medium	0.3	0.05	12	0	0.1	35°	0.57	6
CFS-weak	0.15	0.025	23	0	0.1	25°	0.42	8
CFS-weakest	0.06	0.01	23	0	0.1	15°	0.26	6
CS-weak	0.06	0.0	50	0	0.1	6°	0.10	10
Units			[kPa]	[?]	[GPa]	[deg]	[deg]	[kPa]

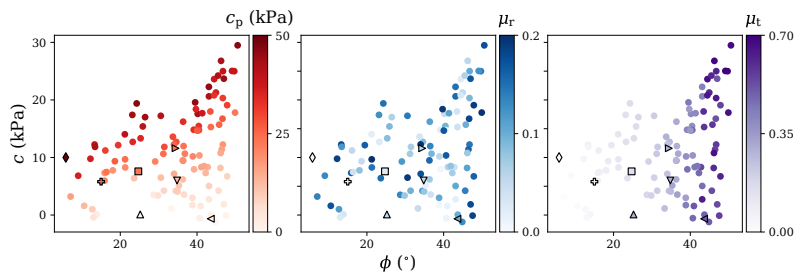


Figure 18: The mapping between the particle parameters of cohesion (left), rolling resistance (middle) and tangential friction (right) to the bulk parameters internal friction angle (horizontal axis) and bulk cohesion (vertical axis) from 100 different numerical soils investigated using the triaxial test. The figure is taken from [63].

The mapping between the particle and bulk parameters from the triaxial test of 100 different numerical soils is visualized in Fig. 18. The symbols indicate the following soils in Table 1: $<$ for FS_strong, \wedge for FS_weak, $>$ for CFS_strong, \vee for CFS_medium, \square for CFS_weak, $+$ for CFS_weakest and \diamond for CS_weak.

4.5 Digging tool parameter validation and calibration

There are three parameters that control the tool-terrain interaction and affect the soil reaction force. The parameters and their default values are *secondary separation deadload limit* (0.2), the *penetration force scaling* (1.0) and *aggregate stiffness multiplier* (1.0), which have the default values 0.2, 1.0 and 1.0, respectively. If the soil resistance force is too small (or large) these parameters can be increased (decreased) in value. If the resistance force has large fluctuations the aggregate stiffness multiplier may need to be decreased.

When there are no available measurement data, the recommended way to do validation and calibration is to perform high-resolution simulations with a fine grained NDEM and rigid multibody simulation, where the soil resistance force is primarily an effect of the geometric shape and motion of the tool as it interact with the particle-based soil. This assumes that the NDEM contact parameters have the suitable values for a desired type of soil. Example of validation simulations are given in Sec. 5.

5 Simulations

The `agxTerrain` model is validated through comparison with simulations of different earth-moving processes performed using a fully particle-based terrain model. The expectation is that the models for the active zone, separation and penetration resistance that is predicted by `agxTerrain` coincides with what emerges automatically in the fully particle-based simulations due to the local contact model and collective force network and bulk flow. These comparison also serve as calibration tests to determine and adjust any parameters in the `agxTerrain` model that are otherwise unknown.

The results in Sec. 5.1 and 5.2 are made using a development branch of `agxTerrain` with improvements on the geometric representation of the digging tool's inner shape and aggregate body contact points. With `AGX 2.28.0.0` and older versions, the difference in tool reaction force between NDEM and `agxTerrain` simulations show much larger deviations (up to 25-50%) than presented here.

5.1 Excavation

Simulations are performed with a primitive model of an excavator arm and bucket digging in a flat bed of terrain. Still images from the NDEM and `agxTerrain` simulations are

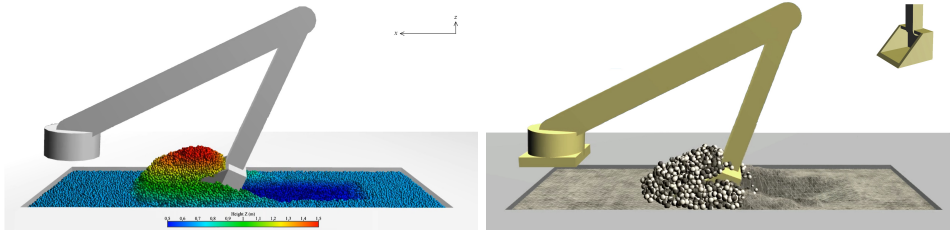


Figure 19: Comparison excavation simulations using NDEM model (left) and `agxTerrain` model (right) for the purpose of validation and calibration.

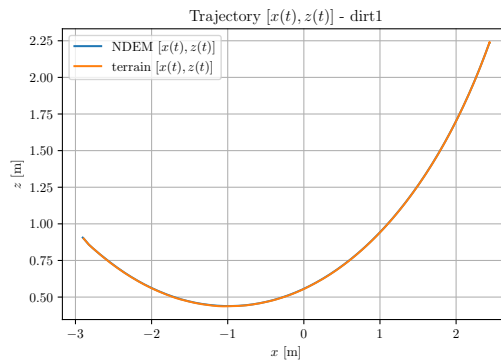


Figure 20: Comparison simulations using NDEM model (left) and `agxTerrain` model (right) for the purpose of validation and calibration.

shown in Fig. 19. The terrain material is set to `Dirt-1` (see Sec. 4.4). The digging motion is realized by controlling the link actuators, by assigning the hinge motor a set angular velocity as function of time. The bucket speed is roughly 0.5 m/s. The motors are assigned a limited maximum torque and will not be able to perform the planned trajectory of the digging resistance become too large.

The NDEM simulation uses 50 mm particles, 1 ms time-step and 250 PGS solver iterations. The `agxTerrain` simulation is run with 10 ms time-step and 0.1 m element size. The number of particles in the NDEM simulation is 200×10^3 while the `agxTerrain` simulation amounts up to roughly 1000 particles and run at realtime performance. The difference in simulation speed is roughly a factor of 2000 times on a i7-8700K 3.7 GHz CPU running 8 threads.

The trajectories of the bucket tip is shown in Fig. 20. The trajectory deviation between the two simulation models is nearly indistinguishable.

The terrain surfaces after the digging cycle are shown in Fig. 21. The negative volume change (the dug hole) amounts to -0.20 m^3 in the NDEM simulation and -0.17 m^3 in the `agxTerrain` simulation. The positive volume changes (the pile and the side berms) are 0.29 m^3 and 0.12 m^3 . The differences are 15 % and 41 %, respectively. The discrepancy in mass is accounted for in the bucket.

The digging resistance forces on the bucket are shown in Fig. 22 for the two different models. The forces are in good agreement after calibration of the *secondary separation deadload limit* to 0.2, *penetration force scaling* to 2.0 and *aggregate stiffness multiplier* to 1.0. The *shovel stiffness multiplier* was calibrated to 0.015. The main difference can be observed during the initial penetration into the soil, during 0.5 to 1.0 s, where the penetration force grows faster in the NDEM simulation than in the `agxTerrain` simulation.

The evolution of the active zone can be seen in seen in Fig. 23. The failure angle is measured to $34 - 41^\circ$ during the bucket filling. This should be compared to the value

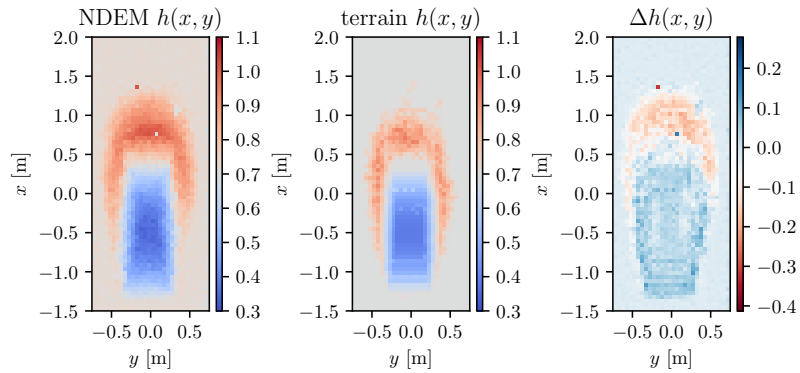


Figure 21: The resulting terrain surfaces after an excavation cycle with NDEM simulation (left), agxTerrain simulation (middle) and their difference (right).

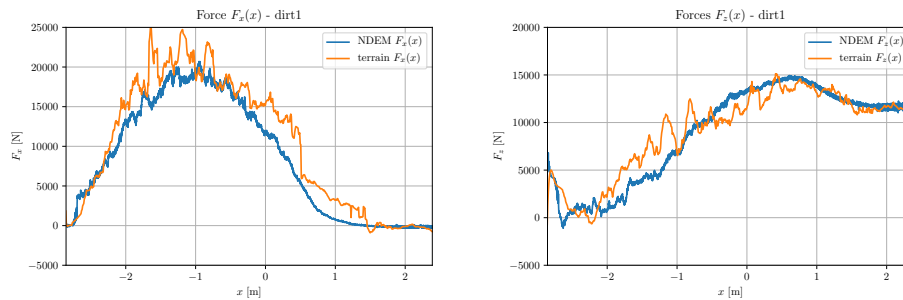


Figure 22: The digging resistance force on the bucket from NDEM (blue) and agxTerrain (orange) split in horizontal (left) and vertical (right) components.

$\theta = 34^\circ$ that is predicted by Eq. (41) with $\phi = 23^\circ$ for **Dirt-1** and $\beta = 90^\circ$ for the planar bed. The model by Park, in Eq. (20), predict $\theta_{\text{Park}} = 23^\circ$.

The active zone is also analyzed for digging in sloped terrain using high-resolution particle-based simulation, see Fig. 24. The failure angle is measured to 41° . The model in Eq. (41) predict $\theta = 44^\circ$ while the Park model predict $\theta_{\text{Park}} = 45^\circ$.

5.2 Bulldozing

Simulations are performed with a blade bulldozing in a flat bed of terrain. Still images from the NDEM and **agxTerrain** simulations are shown in Fig. 25. The terrain material is set to **Dirt-1** (see Sec. 4.4). The blade is attached with a lock constraint to body which motion is controlled via motor constraint. The blade target velocity is 1.0 m/s and the cutting depth is about 0.05 m. The blade is 1.6 m wide and has a mass of 100 kg. It is attached to a kinematic body using a lock constraint. The blade reaction force is measured from that constraint force. The *penetration force scaling* was kept at default 1.0 and so was the *secondary separation deadload limit* at 1.0. The *shovel stiffness multiplier* was calibrated to 0.008.

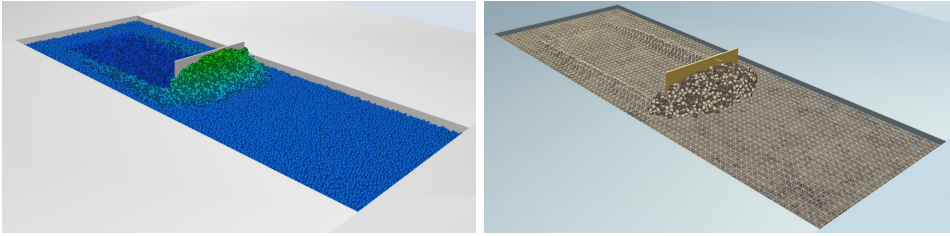


Figure 25: Comparison bulldozing simulations using NDEM model (left) and **agxTerrain** model (right) for the purpose of validation and calibration.

The terrain surfaces after the bulldozing cycle are shown in Fig. 26. The negative volume change (the cut material) amounts to -0.23 m^2 in the NDEM simulation and -0.17 m^2 in the **agxTerrain** simulation. The positive volume changes (the pile and the side berms) are 0.30 m^2 and 0.23 m^2 . The differences are 26 % and 23 %, respectively. The discrepancy in volume correspond to material swelling by 30 % and 35 %, respectively.

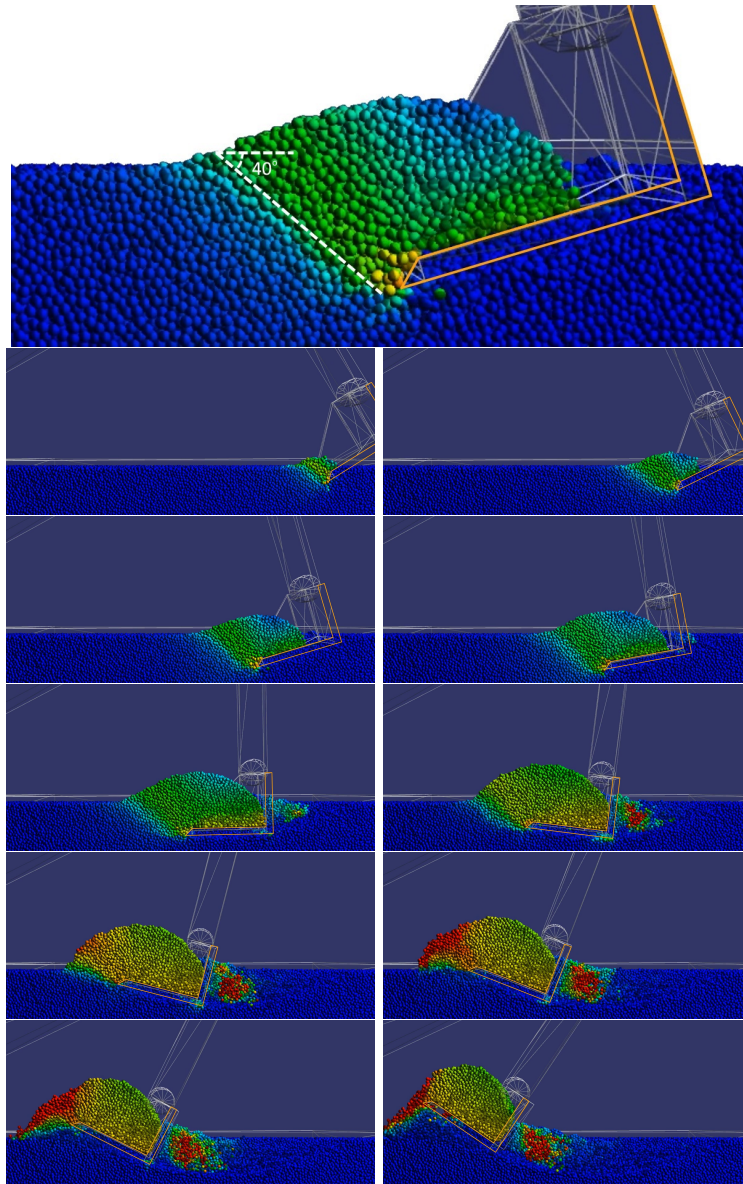


Figure 23: The evolution of the active zone during excavation with the failure angle estimated to $30 - 41^\circ$ degrees. The particles are colour coded with blue to red ranging between 0 and 1 m/s.

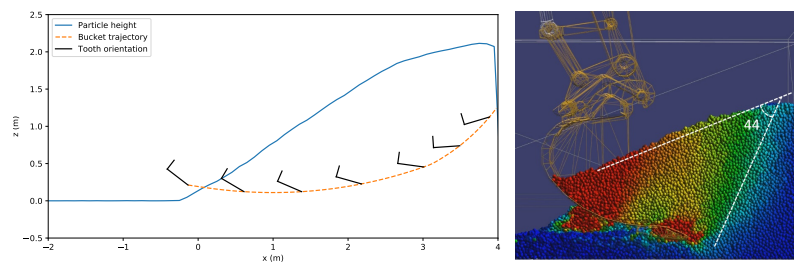


Figure 24: Analysis of the active zone from digging in sloped terrain using particle-based simulation.

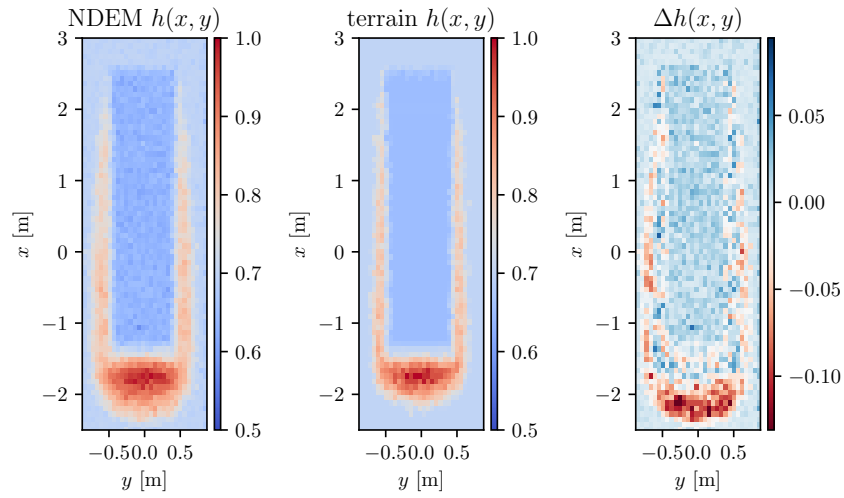


Figure 26: The resulting terrain surfaces after a bulldozing cycle on an NDEM terrain (left) and an agxTerrain (right).

The evolution of the bulldozing sequence and the active zone can be seen in seen in Fig. 27. The failure angle is measured to 30° during the bucket filling. This should be compared to the value $\theta = 34^\circ$ that is predicted by Eq. (41) with $\phi = 23^\circ$ for Dirt-1 and $\beta = 90^\circ$ for the planar bed. The model by Park, in Eq. (20), predict $\theta_{\text{Park}} = 23^\circ$.

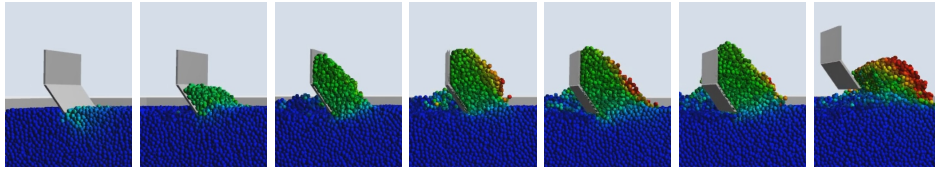


Figure 27: The evolution of the active zone during bulldozing . The particles are colour coded with blue to red ranging between 0 and 1 m/s.

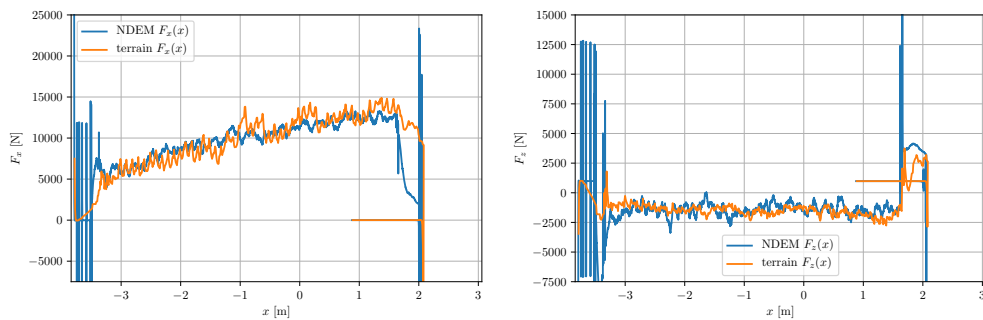


Figure 28: The bulldozing resistance force on the blade from NDEM (blue) and agxTerrain (orange) split in horizontal (left) and vertical (right) components.

6 Conclusions

It is possible to capture complex soil behavior and realistic reaction forces on earthmoving equipment with a multiscale model for dynamic terrain that enables realtime simulation of earthmoving equipment and heavy vehicles. The model combines continuum soil mechanics discretised in fix voxels, pseudo-particles for capturing the flow behavior and a rigid aggregate model for the inertia and strength of the active soil contacting the tool. The result is a relatively low-dimensional model that may be simulated with large timestep and small CPU and memory footprint. In the excavation example in Sec. 5.1 the `agxTerrain` model has 1000 times less number of degrees of freedom and is 2000 times faster to simulate than the corresponding nonsmooth DEM model.

The key parameters are the conventional bulk mechanical properties of the soil. It is important that the pseudo-particle parameters are consistent with the set bulk properties. Therefore, it is advised to rely on a material library that provide such matching sets of parameters, determined from bulk validation and calibration tests performed using nonsmooth DEM simulation.

The realtime model is validated using resolved multibody and DEM simulations of excavation and bulldozing. The soil tool reaction force depends on parameters that are not always known, e.g., the precise geometric shape of the tool. The recommended procedure for determining the proper numerical value for these parameters, is to calibrate them using resolved multibody and DEM simulations using the terrain library.

References

- [1] ACARY, V., AND BROGLIATO, B. *Numerical Methods for Nonsmooth Dynamical Systems: Applications in Mechanics and Electronics*. Springer Verlag, 2008.
- [2] ANCEY, C. Plasticity and geophysical flows: A review. *J. Non-Newtonian Fluid Mech.* 142 (2007), 4–35.
- [3] ANDREOTTI, B., FORTERRE, Y., AND POULIQUEN, O. *Granular Media: Between Fluid and Solid, 1st edition*. Cambridge University Press, 2013.
- [4] AZIMI, A., KÖVECSES, J., AND ANGELES, J. Wheel–soil interaction model for rover simulation and analysis using elastoplasticity theory. *IEEE Transactions on Robotics* 29, 5 (Oct 2013), 1271–1288.
- [5] BELHEINE, N. Numerical simulation of drained triaxial test using 3d discrete element modeling. *Computers and Geotechnics* 36 (2009), 320–331.
- [6] BENNETT, N., WALAWALKAR, A., HECK, M., AND SCHINDLER, C. Integration of digging forces in a multi-body-system model of an excavator. *Proceedings of the Institution of Mechanical Engineers, Part K: Journal of Multi-body Dynamics* 230, 2 (2016), 159–177.
- [7] BLOUIN, S., HEMAMI, A., AND LIPSETT, M. Review of resistive force models for earthmoving processes. *Journal of Aerospace Engineering* 4 (2001).
- [8] BURCH, D. *Estimating Excavation*. Craftsman Book, 1997.
- [9] BUSE, F., LICHTENHELDT, R., AND KRENN, R. Scm - a novel approach for soil deformation in a modular soil contact model for multibody simulation.
- [10] COETZEE, C. Review: Calibration of the discrete element method. *Powder Technology* 310 (2017), 104–142.
- [11] CRAIG, R. *Craig’s Soil Mechanics, Seventh Edition*. Taylor & Francis, 2004.

- [12] ESTRADA, N., AZÉMA, E., RADJAI, F., AND TABOADA, A. Identification of rolling resistance as a shape parameter in sheared granular media. *Phys. Rev. E* 84 (Jul 2011), 011306.
- [13] GODWIN, R. A review of the effect of implement geometry on soil failure and implement forces. *Soil and Tillage Research* 97, 2 (2007), 331 – 340.
- [14] GRAY, J. Particle segregation in dense granular flows. *Annual Review of Fluid Mechanics* 50 (2018), 407–433.
- [15] GRIMA, A. P., AND WYPYCH, P. W. Discrete element simulations of granular pile formation: Method for calibrating discrete element models. *Engineering Computations* 28, 3 (2011), 314–339.
- [16] HÄRTL, J., AND OOI, J. Experiments and simulations of direct shear tests: porosity, contact friction and bulk friction. *Granular Matter* 10 (2008), 263–271.
- [17] HOLZ, D., AZIMI, A., AND TEICHMANN, M. Advances in physically-based modeling of deformable soil for real-time operator training simulators. In *2015 International Conference on Virtual Reality and Visualization (ICVRV)* (Oct 2015), pp. 166–172.
- [18] HUNGR, O., EVANS, S. G., BOVIS, M., AND HUTCHINSON, J. N. Review of the classification of landslides of the flow type. *Environmental and Engineering Geoscience* 7, 3 (2001), 221–238.
- [19] IVERSON, R., AND DENLINGER, R. Flow of variably fluidized granular masses across three-dimensional terrain 1. coulomb mixture theory. *Journal of geophysical research* 106, B1 (2001), 537–552.
- [20] JAISWAL, S., KORKEALAAKSO, P., ÅMAN, R., SOPANEN, J., AND MIKKOLA, A. Deformable terrain model for the real-time multibody simulation of a tractor with a hydraulically driven front-loader. *IEEE Access* 7 (2019), 172694–172708.
- [21] JAKY, J. Pressure in silos. In *2nd Int. Conf. Soil Mech* (Balkema, Rotterdam, 1948), vol. 1, pp. 103–107.
- [22] JANDA, A., AND OOI, J. Y. Dem modeling of cone penetration and unconfined compression in cohesive solids. *Powder Technology* 293 (2016), 60 – 68. Particle Modelling with the Discrete Element Method A success story of PARDEM (www.pardem.eu).
- [23] JOHNSON, K. L. *Contact mechanics*. Cambridge University Press, 1985.
- [24] JOP, P., FORTERRE, Y., AND POULIQUEN, O. A constitutive law for dense granular flows. *Nature* 441 (2006), 727–730.
- [25] KARMAKAR, S., AND KUSHWAHA, R. L. Dynamic modeling of soil–tool interaction: An overview from a fluid flow perspective. *Journal of Terramechanics* 43, 4 (2006), 411 – 425.
- [26] KOTROCZ, K., MOUAZEN, A. M., AND KERÉNYI, G. Numerical simulation of soil–cone penetrometer interaction using discrete element method. *Computers and Electronics in Agriculture* 125 (2016), 63–73.
- [27] KRENN, R., AND HIRZINGER, G. Scm—a soil contact model for multi-body system simulations. In *11th European Regional Conference of the International Society for Terrain-Vehicle Systems - ISTVS 2009* (10 2009).
- [28] LACOURSIÈRE, C. Regularized, stabilized, variational methods for multibodies. *The 48th Scandinavian conference on simulation and modeling (SIMS 2007)*, Göteborg, 30–31 (2007), 40–48.

- [29] LACOURSIÈRE, C., LINDE, M., AND SABELSTRÖM, O. Direct sparse factorization of blocked saddle point matrices. *Para 2010: State of the Art in Scientific and Parallel Computing, Reykjavik, June 6-9* (2010).
- [30] LACOURSIÈRE, C. *Ghosts and machines: regularized variational methods for interactive simulations of multibodies with dry frictional contacts*. PhD thesis, Umeå University, SE-901 87 Umeå, June 2007.
- [31] LIU, S. H. Simulating a direct shear box test by dem. *Canadian Geotechnical Journal* 43, 2 (2006), 155–168.
- [32] LUENGO, O., SINGH, S., AND CANNON, H. Modeling and identification of soil-tool interaction in automated excavation.
- [33] MADSEN, J. *Mobility Prediction of Multi-Body Vehicle Dynamics Handling Simulations on DeformableTerrain*. Doctoral thesis, 2014.
- [34] MCKYES, E. *Soil cutting and tillage*. Developments in agricultural engineering. Elsevier, 1985.
- [35] MITARAI, N., AND NORI, F. Wet granular materials. *Advances in Physics* 55 (2006), 1–45.
- [36] MURTY, K. G. *Linear Complementarity, Linear and Nonlinear Programming*. Helderman-Verlag, Heidelberg, 1988.
- [37] MUSETH, K. Vdb: High-resolution sparse volumes with dynamic topology. *ACM Trans. Graph.* 32, 3 (July 2013), 27:1–27:22.
- [38] NETO, E. D. S., OWEN, D. R. J., AND PERIĆ, D. *Computational Methods for Plasticity: Theory and Applications*. Wiley, Chichester, 2008.
- [39] NORDBERG, J., AND SERVIN, M. Particle based solid for nonsmooth multidomain dynamics. *Computational Particle Mechanics* (2017).
- [40] OBERMAYR, M., ET AL. A discrete element model and its experimental validation for the prediction of draft forces in cohesive soil. *Journal of Terramechanics* 53 (2014), 93–104.
- [41] PARK, B. *Development of a Virtual Reality Excavator Simulator: a Mathematical Model of Excavator Digging and a Calculation Methodology*. PhD thesis, Virginia Polytechnic Institute and State University, Blacksburg, Virginia, October 2002.
- [42] PLASSIARD, J.-P., BELHEINE, N., AND DONZE, F. A spherical discrete element model: Calibration procedure and incremental response. *Granular Matter* 11 (10 2009), 293–306.
- [43] PÖSCHEL, T., AND SCHWAGER, T. *Computational Granular Dynamics, Models and Algorithms*. Springer-Verlag, Berlin Heidelberg, 2005.
- [44] R., M. N. D. On dense granular flows. *EPJ E* 14 (2004), 341–365.
- [45] RADJAI, F., AND DUBOIS, F. *Discrete-element modeling of granular materials*. Wiley-Iste, 2011.
- [46] REECE, A. R. The fundamental equation of earth-moving mechanics. *Proc. of the Institution of Mechanical Engineers* 179 (1964).
- [47] ROUX, S., AND RADJAÏ, F. *Physics of Dry Granular Media*. 01 1998, ch. Texture-Dependent Rigid-Plastic Behavior, pp. 229–236.

- [48] SAURET, A., BALMFORTH, N. J., CAULFIELD, C. P., AND MCELWAINE, J. N. Bulldozing of granular material. *Journal of Fluid Mechanics* 748 (2014), 143–174.
- [49] SERVIN, M., AND WANG, D. Adaptive model reduction for nonsmooth discrete element simulation. *Computational Particle Mechanics* 3, 1 (2016), 107–121.
- [50] SERVIN, M., WANG, D., LACOURSIÈRE, C., AND BODIN, K. Examining the smooth and nonsmooth discrete element approach to granular matter. *Int. J. Numer. Meth. Engng.* 97 (2014), 878–902.
- [51] SERVIN, M., WANG, D., LACOURSIÈRE, C., AND BODIN, K. Examining the smooth and nonsmooth discrete element approaches to granular matter. *Journal for Numerical Methods in Engineering* 97 (2014), 878–902.
- [52] SHABANA, A. A. *Dynamics of multibody systems*, third ed. Cambridge University Press, Cambridge, 2005.
- [53] SHMULEVICH, I., ASAF, Z., AND RUBINSTEIN, D. Interaction between soil and a wide cutting blade using the discrete element method. *Soil and Tillage Research* 97, 1 (2007), 37–50.
- [54] TAMÁS, K., KOVÁCS, A., AND JÓRI, I. The evaluation of the parallel bond’s properties in dem modeling of soils. *Periodica Polytechnica Mechanical Engineering* 60, 1 (2016), 21–31.
- [55] TASORA, A., MANGONI, D., AND NEGRUT, D. An overview of the chrono soil contact model (scm) implementation - technical report tr-2017-01.
- [56] THOENI, K., FITYUS, S. G., GIACOMINI, A., AND VAHA, J. Discrete modelling of a tilt box test for granular materials. In *Computer Methods and Recent Advances in Geomechanics* (2015), Oka, Murakami, Uzuoka, and Kimoto, Eds., Taylor & Francis Group, London.
- [57] TSUJI, T., NAKAGAWA, Y. AND MATSUMOTO, N., AND KADONO, Y. 3-d dem simulation of cohesive soil-pushing behavior by bulldozer blade. *Journal of Terramechanics* 49 (2012), 37 – 47.
- [58] VERRUIJT, A. *An Introduction to Soil Mechanics*. Springer Nature, 2018.
- [59] WANG, D., ET AL. Warm starting the projected gauss-seidel algorithm for granular matter simulation. *Computational Particle Mechanics*. 3, 1 (2016), 43–52.
- [60] WANG, D., AND SERVIN, M. Warm starting the projected gauss-seidel algorithm for granular matter simulation. *Computational Particle Mechanics* 3, 1 (2016), 43–52.
- [61] WANG, D., SERVIN, M., BERGLUND, T., MICKELSSON, K.-O., AND RÖNNBÄCK, S. Parametrization and validation of a nonsmooth discrete element method for simulating flows of iron ore green pellets. *Powder Technology* 283 (2015), 475 – 487.
- [62] WENSRICH, C., AND KATTERFELD, A. Rolling friction as a technique for modelling particle shape in dem. *Powder Technology* 217 (2012), 409 – 417.
- [63] WIBERG, V., AND SERVIN, M. Numerical soil under heavy vehicles. *Submitted for publication* (2019).
- [64] WONG, J. Y. *Theory of Ground Vehicles, 3rd ed.* John Wiley & Sons, 2001.
- [65] WOOD, D. M., AND GRAHAM, J. Anisotropic elasticity and yielding of a natural plastic clay. *International Journal of Plasticity* 6, 4 (1990), 377 – 388.
- [66] YU, H., AND HOULSBY, G. Finite cavity expansion in dilatant soils: loading analysis. *Géotechnique* 41, 2 (1991), 173–183.

Appendix A - Parameters in the cavity expansion model

The model parameters in the cavity expansion model in Sec. 2.3.3 of Yu and Houlsby [66] are Young's modulus E , Poisson ratio ν , internal friction angle ϕ , cohesion c and angle of dilation ψ , tool tip diameter a_0 , tool base diameter a_{\max} and

$$\bar{Y} = \frac{2c \cos \phi}{1 - \sin \phi} \quad (46)$$

$$G = \frac{E}{2(1 + \nu)} \quad (47)$$

$$\bar{\alpha} = \frac{1 + \sin \phi}{1 - \sin \phi} \quad (48)$$

$$\bar{\beta} = \frac{1 + \sin \psi}{1 - \sin \psi} \quad (49)$$

$$\bar{\gamma} = \frac{\bar{\alpha}(\beta_\phi + m)}{m(\bar{\alpha} - 1)\bar{\beta}} \quad (50)$$

$$\bar{\delta} = \frac{Y + (\bar{\alpha} - 1)p_0}{2(m + \bar{\alpha})G} \quad (51)$$

$$\bar{\eta} = \exp \left[\frac{(\bar{\beta} + m)(1 - 2\nu)[\bar{Y} + (\bar{\alpha} - 1)p_0][1 + (2 - m)\nu]}{E(\bar{\alpha} - 1)\bar{\beta}} \right] \quad (52)$$

$$\bar{\xi} = \frac{[1 - \nu^2(2 - m)](1 + m)\bar{\delta}}{(1 + \nu)(\bar{\alpha} - 1)\bar{\beta}} \left[\bar{\alpha}\bar{\beta} + m(1 - 2\nu) + 2\nu - \frac{m\nu(\bar{\alpha} + \bar{\beta})}{1 - \nu(2 - m)} \right] \quad (53)$$

Appendix B - Direct shear simulation data

Results from numerical direct shear experiments to calibrate pseudo-particle parameters to and bulk mechanical parameters. The direct shear test is performed as described in Sec. 4.2 using the nonsmooth DEM. Specifications of the shear cell and default particle properties and simulation settings are given in Table 2, 3 and 3. Images from a simulation is shown in Fig. 29.

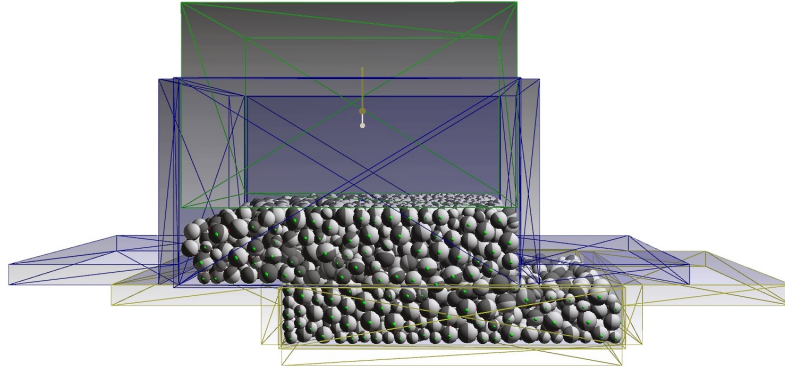


Figure 29: Image from a shear test simulation with the shear cell divided in a load body (green), static top body (blue) and a driven shear body (yellow).

The top body is a static body composed of six composite box geometries that form a void with rectangular cross-section and dimensions $L \times L$. The load body is a single rigid body of mass M_l connected to the top body with a prismatic joint, such that it is free to move in the direction of gravity (up and down). The contacts between the load body and the interior of the top body are disabled (actually the load body is slightly smaller, such that a small gap arises). The shear body is composed of seven box geometries and given

Table 2: Shear cell characteristics.

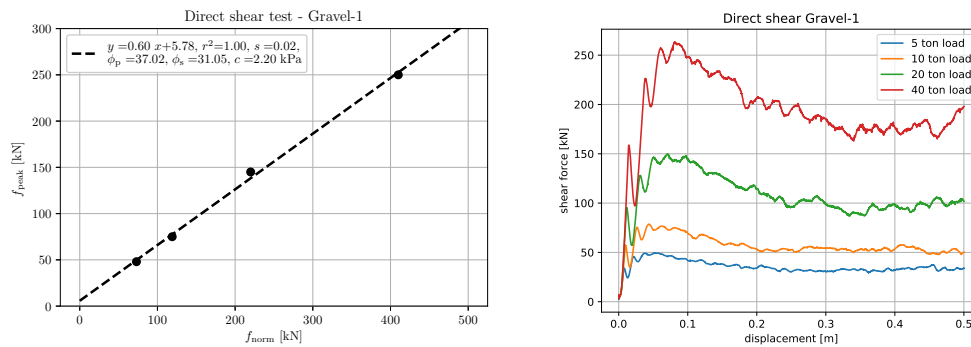
L	~ 1.65 m	inner side length
h	~ 0.6 m	inner height of shear cell
M_l	$[2.5, 40] \times 10^3$ kg	load mass range
v_s	0.1 m/s	shear velocity
σ_h	1.0 kPa	initial hydrostatic pressure

Table 3: Particle characteristics - nominal values.

d	[0.06, 0.85, 0.1] m	particle size
$f_s(d)$	[0.2, 0.3, 0.5]	size distribution
m	[0.2, 0.6, 1.0] kg	particle masses
N_p	$\sim 4k$	number of particles
E_p	10^8 Pa	Young's modulus
μ_t	variable	surface friction ¹¹
μ_r	variable	rolling resistance ¹²
c_p	variable	particle cohesion
d_c	0.005	adhesive overlap

a mass M_s . It is treated either as a kinematic body or a dynamic body, in which case it is constrained with a prismatic joint with a motor, such that its motion in the horizontal shear direction is controlled by a constraint motor producing a constraint force aiming at moving the body at a set target speed v_t . The initial height of the material sample is h and the inner height of the shear body is $h_s = h/2$.

The material is modeled as a granular body system with a contact model that includes elasticity, friction, rolling resistance and cohesion. The particles has size is distributed over three discrete classes: 60, 85, 100 mm. The particle solid mass density is 2000 kg/m^3 . The particle cohesion force limit is derived from particle cohesion c_p in units Pa by multiplying c_p by the particle cross section area.

**Table 4:** Simulation parameters - nominal values.

Δt	0.001	time-step
N_{it}	1500	PGS iterations for coarse and fine

